Keywords: ultra-high energy neutrino detection, radioglaciology, Askaryan effect.

In situ radioglaciological measurements near Taylor Dome, Antarctica and implications for Ultra-High Energy (UHE) neutrino astronomy

D. Z. Besson[1], J. Jenkins[2], S. Matsuno[3], J. Nam[4], M. Smith[2], S. W. Barwick[4], J. J. Beatty[5], W. R. Binns[6], C. Chen[7], P. Chen[7], J. M. Clem[8], A. Connolly[9], P. F. Dowkontt[6], M. A. DuVernois[11], R. C. Field[7], D. Goldstein[4], P. W. Gorham[3], A. Goodhue[9], C. Hast[7], C. L. Hebert[3], S. Hoover[9], M. H. Israel[6], J. Kowalski[3], J. G. Learned[3], K. M. Liewer[11], J. T. Link[1,12], E. Lusczek[10], B. Mercurio[5], C. Miki[3], P. Miočinović[3], C. J. Naudet[11], J. Ng[7], R. Nichol[5], K. Palladino[5], K. Reil[7], A. Romero-Wolf[3], M. Rosen[3], L. Ruckman[3], D. Saltzberg[9], D. Seckel[8], G. S. Varner[3], D. Walz[7], F. Wu[4]

[1]*Dept. of Physics and Astronomy, Univ. of Kansas, Lawrence, KS 66045.* [2]*U.S. Antarctic Program, McMurdo Station, Antarctica.* [3]*Dept. of Physics and Astronomy, Univ. of Hawaii, Manoa, HI 96822.* [4]*Univ. of California, Irvine CA 92697.* [5]*Dept. of Physics, Ohio State Univ., Columbus, OH 43210.* [6]*Dept. of Physics, Washington Univ. in St. Louis, MO 63130.* [7]*Stanford Linear Accelerator Center, Menlo Park, CA, 94025.* [8]*University of Delaware, Newark, DE 19716.* [9]*Dept. of Physics and Astronomy, Univ. of California, Los Angeles, CA 90095.* [10]*School of Physics and Astronomy, Univ. of Minnesota, Minneapolis, MN 55455.* [11]*Jet Propulsion Laboratory, Pasadena, CA 91109.* [12]*Currently at NASA Goddard Space Flight Center, Greenbelt, MD, 20771.*

(Dated: May 6, 2019)

Abstract

Radiowave detection of the Cherenkov radiation produced by neutrino-ice collisions requires an understanding of the radiofrequency (RF) response of cold polar ice. We herein report on a series of radioglaciological measurements performed approximately 10 km north of Taylor Dome Station, Antarctica from Dec. 6, 2006 – Dec. 16, 2006. Using RF signals broadcast from: a) an englacial discone, submerged to a depth of 100 meters and broadcasting to a surface dual-polarization horn receiver, and b) a dual-polarization horn antenna on the surface transmitting signals which reflect off the underlying bed and back up to the surface receiver, we have made time-domain estimates of both the real (index-of-refraction "n") and imaginary (attenuation length "L_{atten}") components of the complex ice dielectric constant. We have also measured the uniformity of ice response along two orthogonal axes in the horizontal plane. We observe an apparent wavespeed asymmetry of order 0.1% between two orthogonal linear polarizations projected into the horizontal plane, consistent with some previous measurements, but somewhat lower than others.

Introduction

The Antarctic icecap is the world's largest stable, homogeneous surface feature, comprising 75% of the current freshwater reserves on the planet. The pristine nature of the ice, with relatively few defects or impurities, results in exceptional transmission properties for both electromagnetic and acoustic/seismic signals. At wavelengths of 300 nm(/1 m), electromagnetic attenuation lengths are of order 200 m(/2000 m)[1, 2].

The lack of substantial human and animal activity on the continent makes the icecap an ideal locale for experimental efforts seeking to measure rare collisions of extra-terrestrial objects, both microscopic[2, 3] and macroscopic (meteorites, e.g.[4]) with the icecap itself. The long scale of signal transmission allows a radio sensor to probe an extremely large volume for englacially generated radiowave signals. In the case where ultra-high energy cosmic-ray neutrinos are measured via the coherent Cherenkov radiation produced subsequent to their collision with ice molecules, ice properties must be understood. In particular, the attenuation, absorption, and possible de-polarization of the resulting electromagnetic signals due to the ice intervening between the interaction point and the detection sensor must be quantified if one is to accurately reconstruct the four-momentum of the initial neutrino. Measurement of Antarctic ice properties over a large footprint is particularly important for the ANITA experiment[5], which seeks to register neutrino-induced radiowave signals using a suite of high-bandwidth horn antennas mounted on a gondola. From a height of 38 km, ANITA monitors a mass of ice out to the horizon 680 km away.

The electromagnetic response of some medium is typically expressed in terms of a complex dielectric 'permittivity' $\epsilon = \epsilon'(\omega, \hat{n}) + i\epsilon''(\omega, \hat{n})$, where ω is the angular frequency and $\hat{n}$ is the polarization vector. The real part of the dielectric constant ($Re(\epsilon) = \epsilon'$) is related to the electromagnetic wavespeed via: $v' = c/\sqrt{|\epsilon'|}$; in the limit of small $\tan\delta$, the imaginary part ($Im(\epsilon) = \epsilon''$) gives the power loss through the medium via: loss (dB/m)=$8.686(\omega/2c_0)(\sqrt{\epsilon'}\tan\delta)$[6]. Here, c_0 is the electromagnetic wavespeed *in vacuum*, and $tan\delta = \epsilon''/\epsilon'$.

The response of ice as a function of polarization ("birefringence") has been probed with a variety of measurements[7, 8, 9, 10, 11, 12]. Asymmetries are characterized as differences in either wavespeed or absorption along linear (generally orthogonal) axes. Formally, the two asymmetries ($\delta_{\epsilon'}$, real and/or $\delta_{\epsilon''}$, imaginary) are linked by the Kramers-Krönig dispersion relation – if one is non-zero the other must be non-zero, as well. In the absence of any preferred in-ice direction, one might expect any asymmetry to be mitigated by the random-walk nature of the birefringence. In such a case, over a total pathlength l consisting of N unit steps, each of which is characterized by an asymmetry b, the average propagation time for each polarization axis should have a Gaussian distribution, centered at l/c, with width $b\sqrt{N}l/Nc$. The asymmetry distribution would therefore be a Gaussian of width $\sigma_b = b\sqrt{2N}l/Nc$, centered at zero. For 1% birefringence ($b = 0.01$), l=1000 m, and values of distance scale corresponding to typical grain sizes (10^{-3} m, or N=10^6), we expect $\sigma_b \lesssim$0.1 ns. By comparison, typical neutrino-induced signal durations measured by ANITA are of order 3-4 ns, so this difference is insignificant.

The impedance mismatch of air relative to ice, or ice relative to bedrock introduces non-zero reflections at that interface. The corresponding reflection and transmission coefficients, for the perpendicular and parallel components of planar incident electric field wavefronts ($r_\perp$, $r_{||}$, $t_\perp$ and $t_{||}$, respectively), are given by the standard "Fresnel equations for dielectric media", in terms of the angle-of-incidence (θ_i) and angle-of-transmission (θ_t), and the index of refraction ($n(\omega, \hat{n}) = \sqrt{\epsilon'(\omega, \hat{n})}$). For ANITA, the change in dielectric from below the firn up through the surface interface (i.e., air-ice) largely determines the volume of ice visible to the balloon. For constant voltage threshold V_{thresh} (and neglecting absorption), the minimum field strength observable from the balloon is given by $E_0 R = V_{thresh}$, where E_0 is the strength of the signal at the production point, R is the distance from production point to observation point and V_{thresh} is the voltage threshold at the detector, typically set to be at least three times the ambient thermal noise background, or: $V_{thresh} \sim 3V^{rms}_{thermal\ noise}$. For large values of E_0, the observable volume is (neglecting the 38 km altitude of the balloon, and taking R to be measured in the horizontal plane) disk-like. In this case, most of the sensitive volume is at the edge of the horizon and the angles of incidence relative to the balloon are close to the critical angle.

Scope of Experimental Work

Our primary goal was to perform measurements important to understanding radiowave propagation through the ice, refracted at the surface, and ultimately received by the ANITA gondola. To that end, a series of studies were conducted, as summarized in Table I.

Measurement	Transmitter→Receiver Configuration	Geometry	Implications
L_{atten} ($Im(\epsilon)$)	Surface horn→surface horn reflected off bedrock	"V"-axis≡14.8 degrees E of true N; in horizontal plane	Range of observable neutrino interactions
Birefringence	(same)	(same)	ANITA trigger efficiency
$n(z)$ ($Re(\epsilon)$) ≡Index-of-refraction as f(depth)	in-ice discone→surface horn	"V"-axis≡vertical c-axis	$\theta_{critical}$, ray-tracing through ice/firn
Surface Roughness	(same)	(same)	Signal amplitude at gondola

TABLE I: Scope of radioglaciological measurements carried out at Taylor Dome. The "V" axis defines antenna orientation, and is detailed elsewhere in the text.

Experimental Technique

Geometry

The geography of the NASA Core Site camp is presented in Figures 1 and 2 (tip of green arrow). As indicated in Table I, the orientation of the antennas is denoted by the two orthogonal linear polarization 'V' and 'H' axes. If both transmitter ("Tx") and receiver ("Rx") are aligned with 'V', the orientation is therefore described as 'VV', e.g. In the other case of the vertically-oriented in-ice discone broadcasting to a surface receiver, only the polarization of the receiver horn is indicated ("Hpol" or "Vpol", e.g.). For the in-ice measurements described below, the VV-axis is approximately 14.8 degrees East of true North, and points roughly in the direction of the primary Taylor Dome base. Over a distance scale of ∼10 km, the VV axis approximately coincides with the surface elevation gradient over that scale. Over a shorter distance scale (∼0.5 km), the HH-axis coincides roughly with the more local surface gradient.

Transmitted Signal Characteristics

Signals are produced using a high-power (2.5 kV peak-to-peak voltage) fast pulse generator; the pulser output signal is shown in Figure 3. A short 30-meter, low-loss 0.5-inch thick coaxial cable connects the pulser output to a Seavey quad ridge dual-polarization transmitting horn antenna (Seavey Engineering model QRG-218A), with separate connections along the orthogonal V- and H- axes. Isolation between the two polarizations is typically ≥14 dB (power). This antenna offers excellent response in the range 200 MHz–1.5 GHz, and is identical to those mounted on the ANITA gondola. The in-air average boresight gain has been measured to be 10 dBi, with a full beamwidth of ∼45 degrees. For the (effective) attenuation length (L_{atten}) measurements described below, signals were directed either downwards and reflected off the underlying bedrock to an identical receiver surface antenna, or parallel to the ice surface, with both antennas facing each other through-air, to provide a normalization for the in-ice reflected signal. (It is important to emphasize here that we measure the average, or "effective" attenuation length averaged over ice of varying temperature, whereas the attenuation length relevant to neutrino detection is primarily that of cold [$T \sim -50$ C] polar ice.) For reflection off the bedrock, the receiver horn signal was first high-pass (Minicircuits model SHP-150) filtered and then immediately amplified by 20 dB in power to enhance the signal voltage (Figure 4). In the configuration where the surface receiver measures signals broadcast from an in-ice discone (designed and constructed at the University of Hawaii), the surface horn is inclined downwards at a cant angle of 11 degrees below the horizontal, unless otherwise specified. The discone was lowered into a ∼12 cm diameter hole, drilled to a depth of 100 m in November, 2006, by the 2006-07 ITASE drilling team.

Following reception at the receiver horn, signal is conveyed through ∼100 m of low-loss coaxial cable to a 3 GHz-bandwidth Tektronix TDS694 digital oscilloscope, which performs waveform capture at 2.5 GSa/sec. For most of the measurements described herein, we average over multiple samples (∼60-2000, depending on the measurement). The single-shot jitter is observed to be approximately 200 ps in time, and 5% in peak voltage.

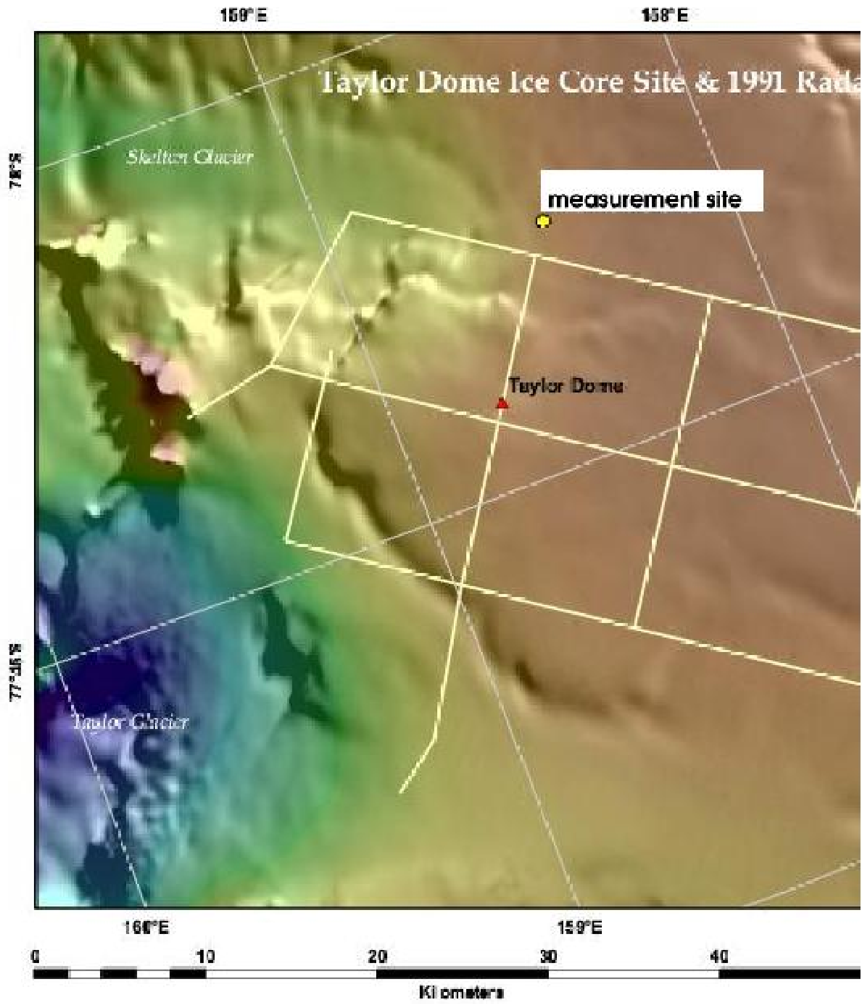

FIG. 1: Coordinates of measurement site (yellow circle) and main Taylor Dome base (red triangle)

Procedure

Measurement of Attenuation Length

Attenuation of radiofrequency signals is impurity and temperature-dependent, and shows large variations across the Antarctic continent. A recent frequency-domain RF attenuation length measurement at SIPLE Dome in West Antarctica, for example, gave an average field attenuation length value of L_{atten} ~238–334 m[15] in the range ~5 MHz, considerably smaller than a time-domain measurement at South Pole[2]. This lower average attenuation length is not entirely unexpected, given the relatively warm ice temperature profile in West Antarctica and the proximity to the ice sheet at the former location. The ANITA sensitivity is dominated by the interior ice.

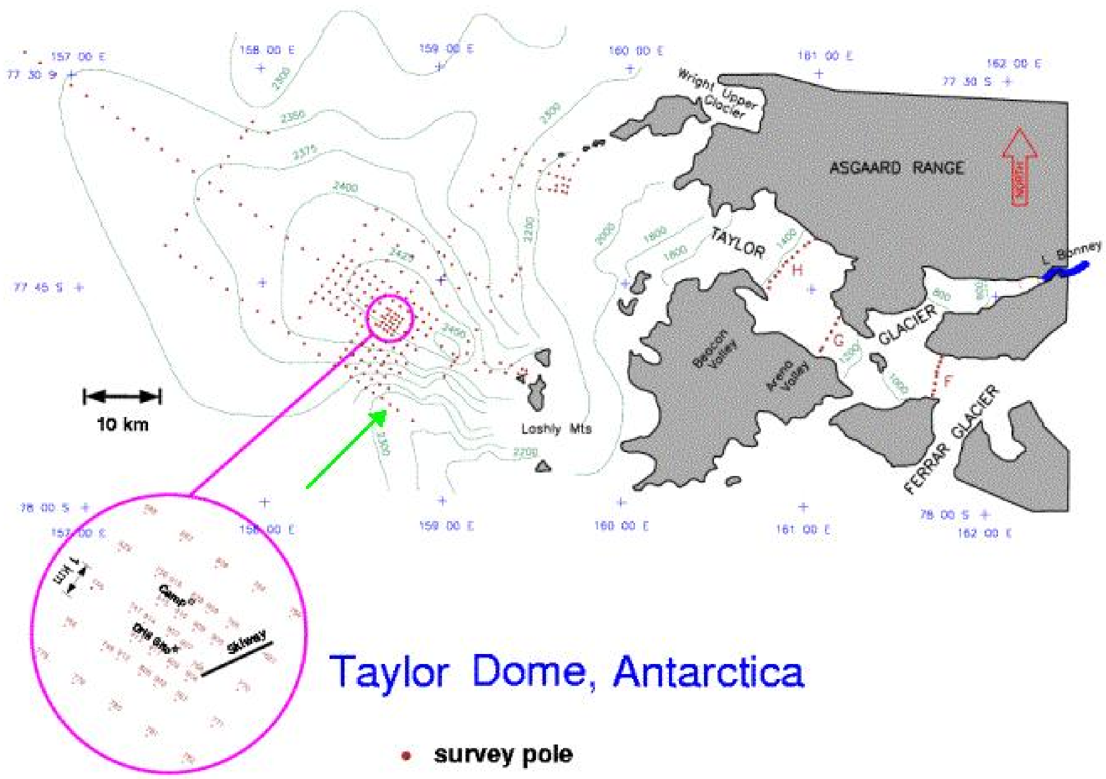

FIG. 2: Topographical map of experimental site. Measurements were made at location corresponding to tip of green arrow.

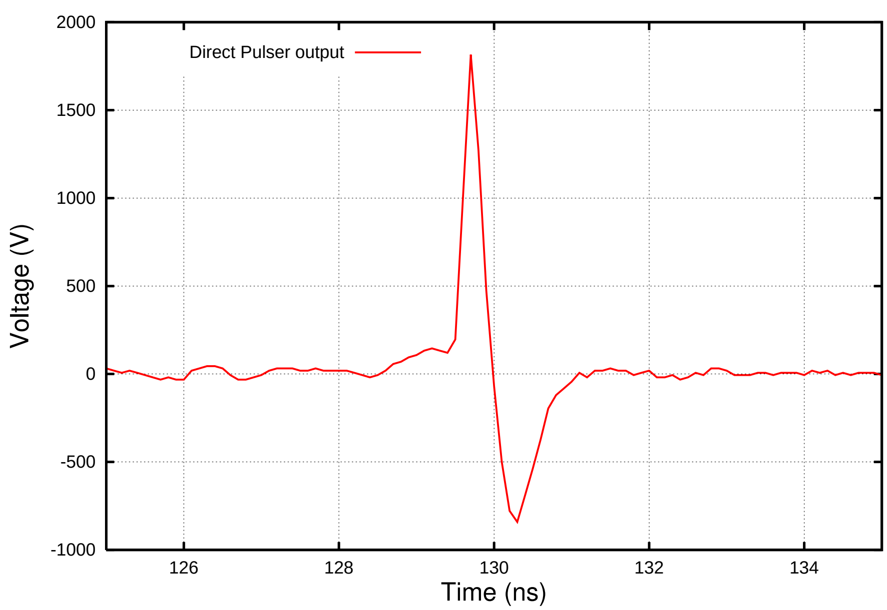

FIG. 3: Pulse generator output signal. Horizontal time offset from zero is arbitrary.

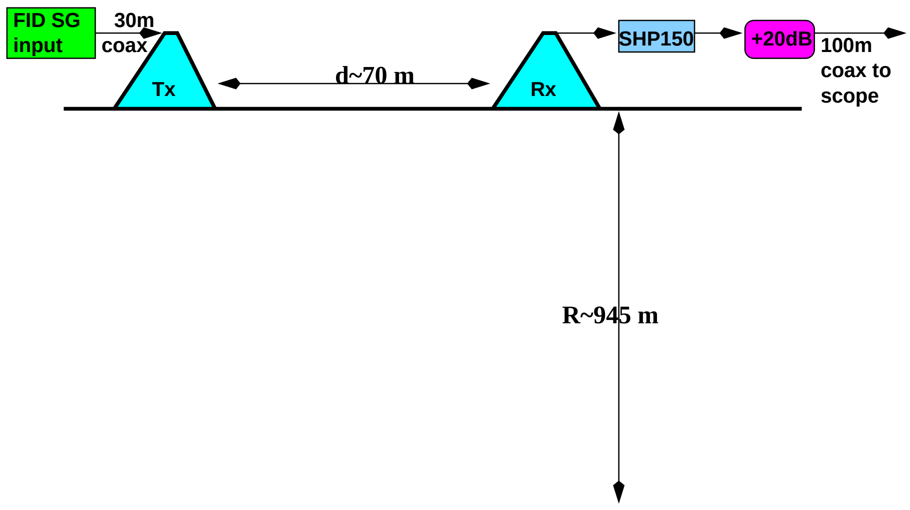

FIG. 4: Set-up used for experimental measurement of bottom reflection. For in-air transmission ("S_{12}(air)"), horns face each other on the surface. Bottom reflection measurements were also made with the receiver horn antenna displaced ~100 m to the left of the transmitter, as described later in this document.

Received Power Magnitude and L_{atten} Determination

Two complementary calculations permit an estimate of the average ice radiofrequency attenuation length at our site. First, we compare the signal amplitude V_{ice} measured through the in-ice path (S_{12}(ice)) normalized relative to the signal amplitude V_{air} measured when the transmitting horn broadcasts along boresight to the receiver horn in-air (S_{12}(air)). Knowing the distance between the horns in-air (d_{air}) and the round-trip distance of the signal path through ice d_{ice}, and attributing all losses greater than (assumed spherical) 1/r amplitude spreading to ice attenuation, we can use $V_{ice}/V_{air} = (G_{ice}/G_{air}) \times (d_{air}/d_{ice})e^{-d_{ice}/\langle L_{atten}\rangle}$ to extract the mean field attenuation length $\langle L_{atten}\rangle$. Implicit in this expression is the assumption that the voltage decreases as 1/r; i.e., that the reflection off the bedrock is coherent. We consider the validity of this assumption later. Here, G_{air} and G_{ice} are the gains for transmission through-air and through-ice, respectively. Since the beamwidth decreases, directivity, or forward gain, increases in the higher-dielectric medium. In our case, assuming the antennas are horizontal on the surface to within 0.1 radians, and the antennas "see" only ice, $G_{air}/G_{ice} \sim$ 10 dBi/15 dBi.

Second, rather than normalizing to the in-air signal, we can "dead reckon" the expected signal at the antenna using the Friis equation. Knowing the total cable length (~125 m), the cable loss per unit length (~5 dB/100 m at 500 MHz), the maximum signal amplitude at the output of the pulser (2.5 kV), the measured reflected signal amplitude V_{ice}, the bandpass of the antennas (~1 GHz), the net gain of the amplifiers + filters in the system (+~18 dB), and the forward in-ice gain of the horn antennas, we can determine "absolutely" the average attenuation length.

S_{12}(air) measurements

For the in-air path, signals were broadcast over a variety of separation distances. To ensure that the trigger signal does not saturate the amplifier, the output of the signal generator was attenuated by 20 dB (power); by contrast, for broadcasts through ice, the signal from the receiver antenna was amplified by 20 dB (power). The raw received signals shown for HH and VV are comparable (Figures 5 and 6; in these and subsequent figures, unless explicitly indicated, waveforms have not been corrected for cable attenuation.). By contrast, cross-talk (VH or HV) is observed to be $\lesssim$10% in voltage amplitude (Figure 7). We note that the amplitudes for HH and VV are quite comparable (Figure 8). Overlaid on the VV- and HH- datasets is the expectation that the signal amplitude should decrease as 1/r for 3-dimensional spreading of spherical wavefronts. We observe deviations of ~25% from this naive expectation, which translates into an uncertainty of order 10% in our extracted field attenuation lengths. Although the far-field approximation should be valid for all these data, the closeness of the antennas to the ice-air boundary and multipath interference effects may complicate interpretation of the in-air data. We consider possible interference effects now.

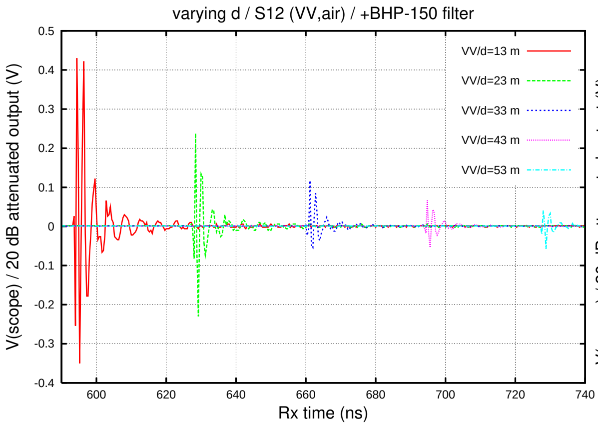

FIG. 5: VV signal observed for in-air transmission, as a function of separation between transmitter and antenna. Overlaid is the expectation that, in the absence of interference effects, the amplitude should vary as 1/r. Note that the extracted propagation velocity agrees with c to within 2% (50 m/134 ns).

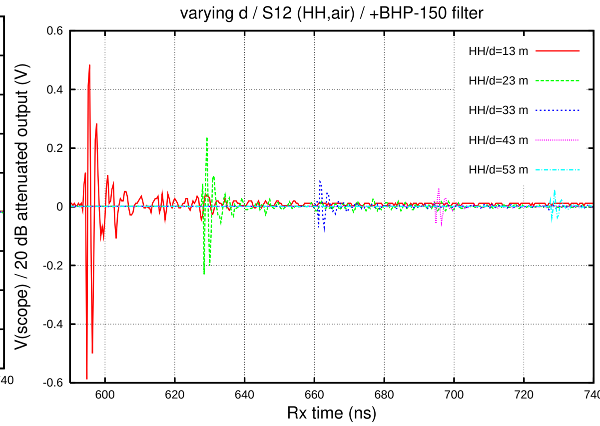

FIG. 6: HH signal observed for in-air transmission, as a function of separation between transmitter and antenna. Relative transmitter and receiver geometry identical to that for the previous Figure; only the broadcast polarization has been changed.

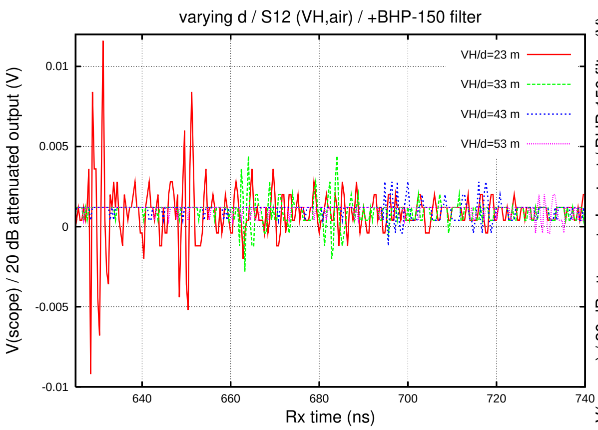

FIG. 7: HV signal observed for in-air transmission, as a function of separation between transmitter and antenna.

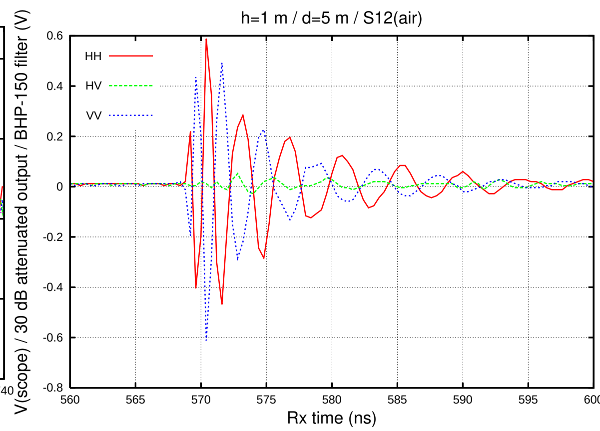

FIG. 8: Comparison of in-air signal strength observed for VV and HH with both Tx and Rx elevated approximately 1 m above snow surface.

Interference considerations for through-air broadcasting.

In principle, the characteristics of the received through-air signal are polarization dependent. There may be interference between a direct-path and an optical path corresponding to reflection off the snow surface. Defining "V" here as the vertical axis perpendicular to the surface ($\hat{z}$), and "H" as the horizontal axis perpendicular to both "V" and the propagation vector, we note that the magnitude of interference in VV vs. HH will differ, since the electric field vector components parallel and perpendicular to the air-ice interface have different, angle-dependent reflection coefficients, as prescribed by the Fresnel equations. At the Brewster angle ($\tan\,\theta_B = n_{ice}/n_{air}$), e.g., the transverse amplitude approaches zero and the reflected angle is longitudinally polarized. Such effects can, in principle, be probed by varying the separation distance between transmitter and receiver over a scale comparable to a wavelength. To assess interference, we made a set of measurements with the two antennas relatively close to each other (d=5 m), and both with and without 1-meter high elevating ice blocks. In general, the time difference between the direct path and the air-surface reflected path is given by: $c\Delta t = 2(\sqrt{h^2+d^2/4}-d/2) \approx 2h^2/d$. Assuming the phase center of the antenna is at a height of 0.5 meters, corresponding to no ice blocks, we obtain $\Delta t \sim 0.333$ ns. For

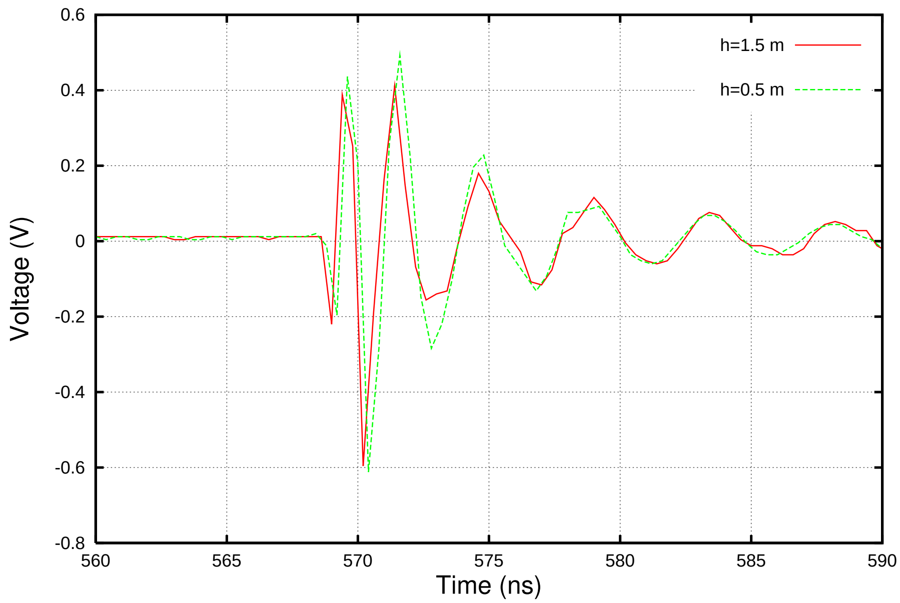

FIG. 9: Comparison of broadcasting in-air (VV) with h=0.5 meters vs. h=1.5 m, corresponding to antennas resting on the snow surface, and elevated by one meter, respectively. The absence of large differences between the two signals indicate that interference effects between the direct path and the path reflected off the air-snow interface are not substantial. Note that, for h=1.5 m, the surface reflection is approximately one beamwidth off boresight.

the case where the antennas are elevated by an additional 1 meter, then $\Delta t \sim$3 ns, corresponding to approximately a phase difference of 3π radians at 500 MHz. Figure 9 shows the comparison for these two elevations. The magnitude of the observed differences indicates that interference between the two possible paths is not substantial. This conclusion is also supported by Figure 8, which shows good agreement between the signals observed for the two polarizations (albeit with a phase shift of π radians) in the elevated configuration.

Comment on surface propagation

It has been suggested[16] that "surface waves", or evanescent solutions to Maxwell's Equations, may offer a promising technique for detection of neutrino-induced radiowave signals. In this model, neutrino-ice collisions in the ice sheet result in radio waves directed towards the surface, which then propagate along the surface with relatively little attenuation, towards suitably located surface receivers. Such z-polarized (Vpol, in our case) signals would be 'trapped' on the air-ice boundary and therefore have an amplitude dependence varying as $\sqrt{r}$. Our S_{12} measurements indicate no preference for Vpol vs. Hpol, and are more consistent with spherical 1/r amplitude diminution.

S_{12}(ice) measurements - signal amplitude

Antennas were initially oriented relative to the local elevation gradient, which is presumed to coincide with the local ice flow axis, pointing in the direction of Taylor Valley, approximately 50 km away.

Estimate of ice depth at Measurement Site

To determine the attenuation length, we must first estimate the ice depth. From the time delay between the sent and the received signal, we can estimate the depth of the ice shelf at the measurement site. We use Taylor Dome ice density data tabulated elsewhere[17] to account for the variation in wavespeed with density, and assume an exponential density profile beyond 100 m, as shown in Figure 10. Also overlaid are preliminary data provided

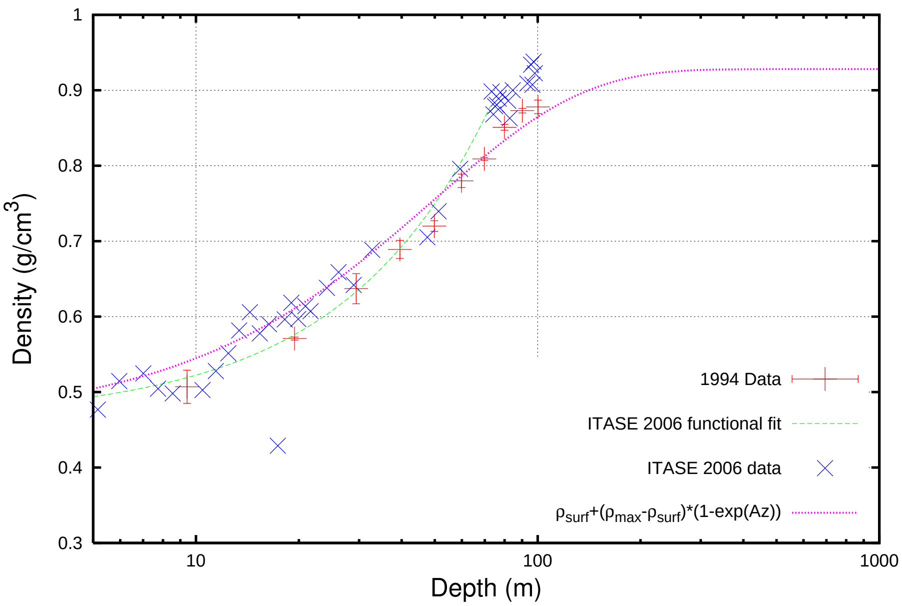

FIG. 10: Density data, taken at Taylor Dome[17], at the our borehole site[18], and functional form of assumed density profile, extrapolated to bedrock.

by the ITASE group based on cores extracted at the time of the November, 2006 drilling[18]. Given the errors, we take these data as qualitatively consistent with the more precise Taylor Dome density data. Comparing the travel time difference for the in-air vs. in-ice measurements (cable delays are the same for both), and knowing the in-air tabulated separation distances, the cable delay offset can be cancelled. Calculating an in-ice transit time of 11100 ns (corrected for cable delays, and based on the average of the HH and VV signal return times; the discrepancy between these corresponds to a depth uncertainty of order 2 meters), we obtain an estimated depth of 940±15 m, where the systematic error shown is dominated by the unknown density profile below 100 m. This value is consistent with other estimates, albeit at ∼5 MHz[19]. (In principle, the equality of the signal propagation times at 5 MHz vs. 500 MHz can be used to bracket the dispersive characteristics of ice over two decades in frequency. The timing resolution δt, however, is expected to follow $\delta t \sim 1/f$.) Knowing the pathlength of the radiofrequency signal through ice, we can now use this value to extract the average ice attenuation length L_{atten}.

Numerical Extraction of Attenuation Length

Comparison of S_{12}*(ice) to* S_{12}*(air) power spectra*

We compare the signal observed over the path-length of the in-ice signal with the signal observed through-air. Figure 11 shows the power spectrum of the through-air signal. We observe considerable power at high frequencies (up to 1 GHz), over a timespan of 10 ns. By contrast, the through-ice received signal is apparently extended by nearly two orders of magnitude. Figure 12 shows a typical reflection signal. Additional V(f) plots for the through-ice signals are shown in Figures 13–16. We typically observe similar spectral content, compared to the S_{12}(air) signal, only for the first 50 ns of received signal. Our power spectra data are also qualititatively consistent with both ice absorption increasing with frequency, as well as the $1/\lambda^4$ dependence characteristic of Rayleigh scattering.

Uncertainties in the frequency dependence of electromagnetic wavespeed in polar ice are also sufficient to allow dispersive effects as a possible explanation for the dilated received signal structure. In that case, our data would be consistent with $dn/d\omega < 0$ in the frequency range of interest. However, it should be noted that, within the limits of our timing resolution (∼100 ns), our previous experiment at South Pole[2] showed very similar signal arrival times for 320 MHz vs. 700 MHz over a total propagation time of 33μs. By contrast, our Taylor Dome data indicate received signal durations of order 120 ns, relative to a total transit time of 11.1 μs.

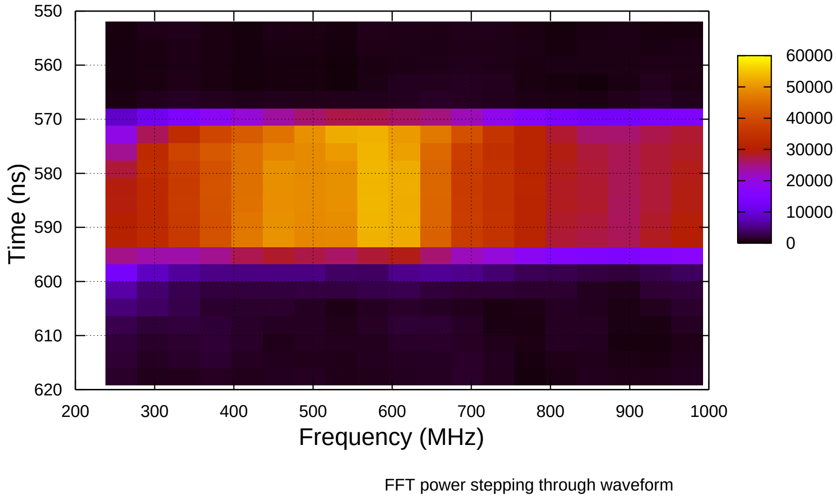

FIG. 11: V(f) characteristics of S_{12}(air) signal (400 ps/sample). z-axis has dimensions [V/MHz]; absolute normalization is arbitrary. To obtain this plot, we have calculated the Fourier transform of V(t) for the through-air received pulser output signal as we step through the waveform.

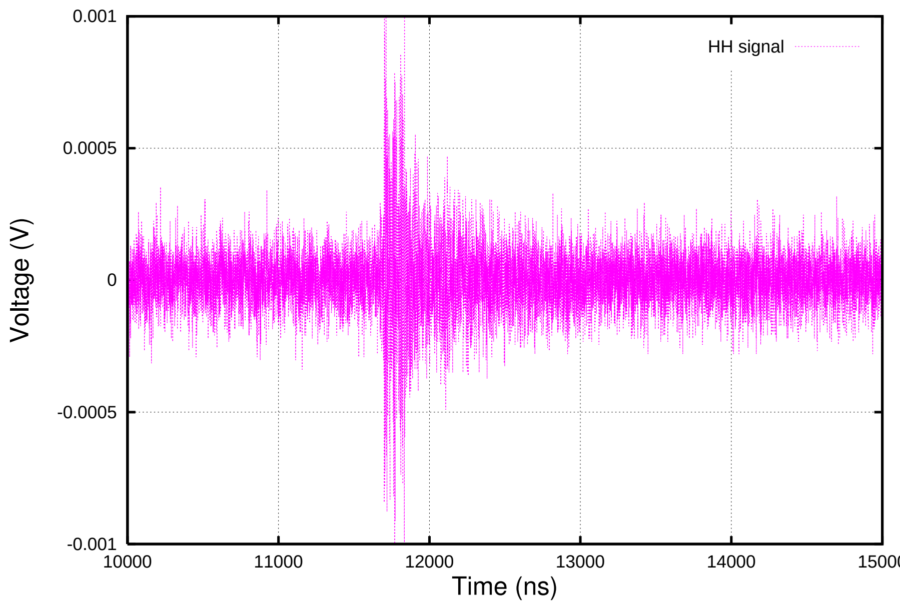

FIG. 12: Typical observed HH reflection signal.

We first extract the attenuation length using the relative signal strengths observed for in-air vs. in-ice broadcasts. To minimize relative distance measurement error, we normalize the S_{12}(ice) signal voltage to the S_{12}(air) signal measured for maximum in-air separation. We compare the calculated attenuation lengths based on: a) the first 10 ns of enhanced voltage amplitude observed in the reflected signal V_{max}, b) the calculated integral of the signal strength, using 50 ns of both in-ice and in-air data, based on the similarity of the broadcast vs. received frequency spectra over this timescale, and c) integrating 250 ns after the initial observed reflection appears to

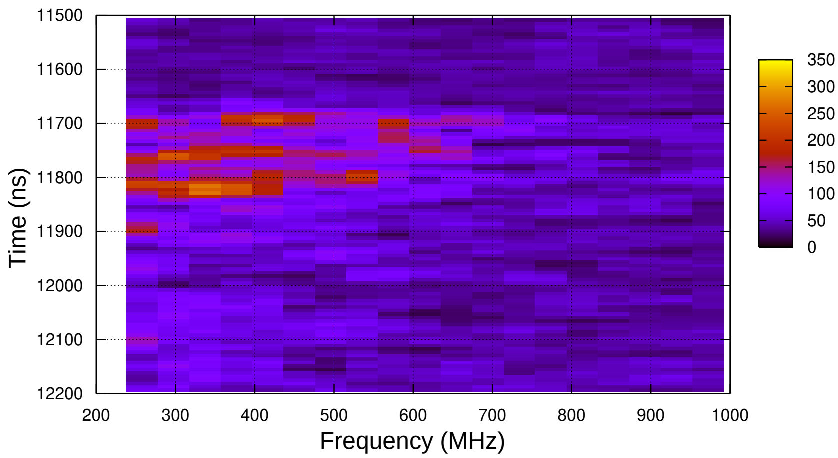

FIG. 13: VV Reflected signal spectral power.

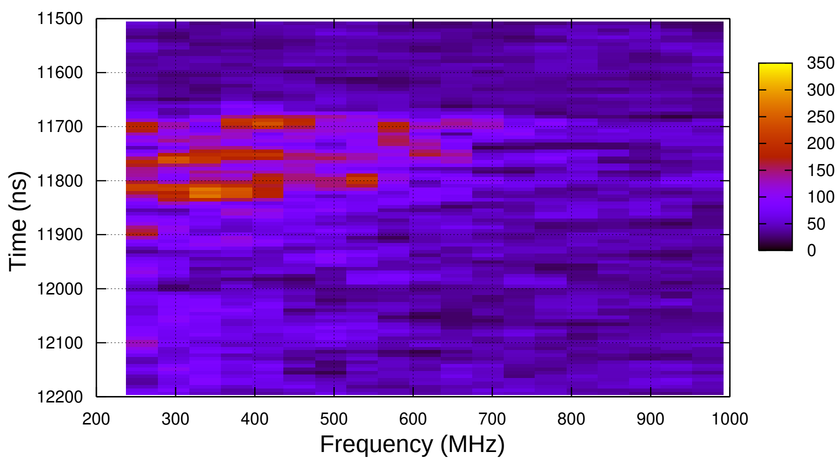

FIG. 14: HH Reflected signal spectral power.

include the entire observed reflection enhancement. For these estimates, we must directly subtract the average voltage $\langle V \rangle_{pre-signal}$, as measured for one microsecond just before the arrival of the reflected signal. Additionally, the ambient rms voltage $\sigma_{V,pre-signal}$ must be subtracted in quadrature. The corrected calculated signal voltage $V_{signal} = \sqrt{(V_{measured,scope} - \langle V \rangle_{pre-signal})^2 - \sigma^2_{V,pre-signal}}$.

Alternatively, these values are determined from direct application of the Friis Equation, as outlined previously.

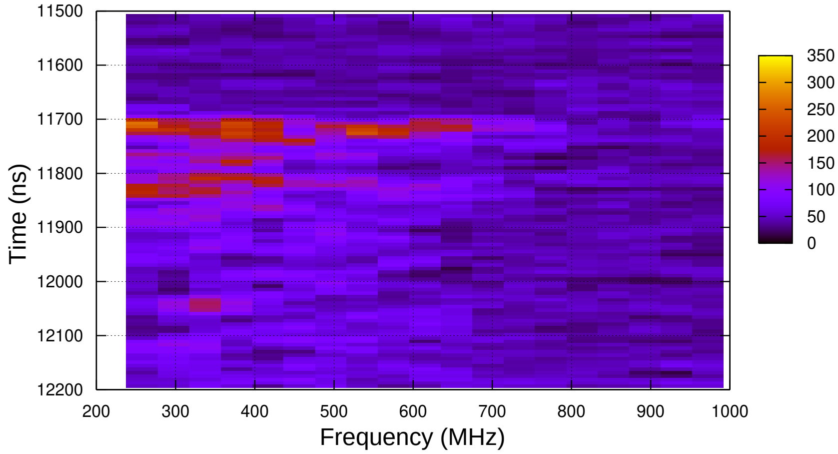

FIG. 15: 'Rotated' VV reflected signal spectral power. Here, the antenna is rotated in the horizontal plane from the initial VV orientation into the HH orientation.

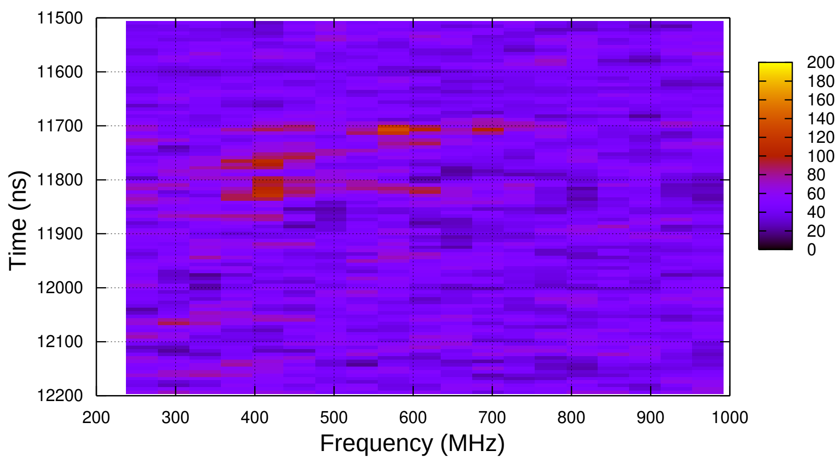

FIG. 16: VH 'cross-polarization' reflected signal power.

Uncertainties in surface scattering at the bedrock

The nature of the bottom reflection critically affects the magnitude of the received signal. In the extreme case, one might assume a mirror-like bottom reflectivity of unity. A more realistic value of reflection coefficient, corresponding to a typical rock-ice dielectric contrast, is approximately 0.3.

Average bottom slope and BEDMAP elevation data.

A bottom surface which is linear in elevation slope, either positive or negative, has the effect of reducing the net estimated signal, as does a concave upwards surface (i.e., a local 'hill'). A concave downwards bedrock surface (i.e., a local 'depression') could have a focusing effect. In our calculation, we have ignored such possible curvature effects. The BEDMAP group has tabulated estimated bedrock[20] and ice surface elevations across the Antarctic continent. Over 5 km$\times$5 km grid squares in the vicinity of our measurement site, surface and bedrock elevations are shown in Table II. The average slope of the bedrock over the area where our measurements have been made is very slight, of order 5 mrad, although local variations exceeding that cannot be ruled out without further measurements.

TABLE II: Surface/Bedrock elevations (BEDMAP). Borehole site has coordinates $\approx$ (1 km,2 km) relative to given grid center coordinates.

x0 (km)	y0 ($\equiv$Grid North) (km)	Surface/Bedrock elevation (m)
-5	-5	2232/1491
-5	0	2185/1372
-5	5	2194/1302
0	-5	2305/1512
0	0	2275/1424
0	5	2291/1379
5	-5	2350/1464
5	0	2353/1422
5	5	2353/1393

Bedrock features

The signal magnitude is sensitive to the scale of the roughness (i.e., surface features, or inhomogeneities) at the bedrock. We expect that, if the bottom surface were characterized by roughness of typical vertical scale h, then the observed signal should be specular and completely coherent for $\lambda \gg h$ and show a loss of coherence for $\lambda \ll h$. In the former case, the specular signal from the horn transmitter is coherent over a bedrock disk ("Fresnel zone") of radius $R \sim \sqrt{2\lambda d_{Tx} d_{Rx}/(d_{Tx}+d_{Rx})}/2$, corresponding to the region over which the phase variation is $< \pi/2$ radians. Here, $d_{Tx} = d_{Rx}$ is the distance from the transmitter or receiver through the ice to the bedrock and λ is the observed wavelength. For $d \sim$1000 m and $\lambda \sim$1 m, then $R \sim$30 m, $R \sim \sqrt{\lambda d_{Tx}}$, corresponding to a maximum smearing in the time domain of approximately 2 ns due to the non-zero size of the illuminated disk. Beyond that region, there will be coherent Fresnel zones at larger radii, with an expected diminution in amplitude.

In the idealized limit of completely incoherent scattering (we assume no depolarization), the high-frequency, low-wavelength power would scatter with a $1/R^4$ dependence off the bottom, vs. a sharper $1/R^2$ dependence for coherent specular reflection. The observed time duration of the reflected signal (Figure 12) implies an illuminated region roughly 10$\times$ larger than our 30-meter estimate above. For incoherent scattering, we expect signal to arrive at the receiver over a timescale dictated by the beamwidth in-ice ($\pm$12 degrees), corresponding to approximately 250 ns given the measured bedrock depth. Our data therefore suggest a substantial fraction of incoherent scattering at the bedrock. To assess the signal amplitude reduction due to loss of coherence, we have calculated the voltage reduction as a function of the scale of the surface scattering at the bedrock, as illustrated in Figure 17. This scale, relative to the typical wavelength scale, determines the fraction of signal which scatters coherently vs. incoherently at the bedrock. For the calculations of attenuation length presented below, our "Incoherent" assumption corresponds to an incoherent fraction of 0.25.

Previous Bottom Reflection Data

We have also used previous data, taken at the South Pole in January, 2004 with similar apparatus, for possible evidence of an extended reflected signal time duration relative to the transmitted signal[2]. (Since the antenna orientation relative to ice flow was not noted, and since data were only taken in the "co-pol" alignment, with Tx

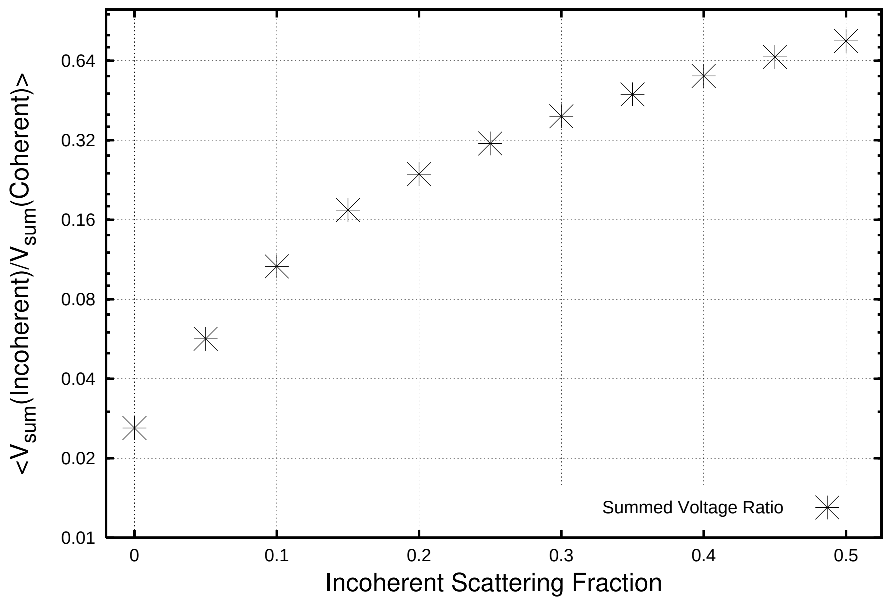

FIG. 17: Expected ratio of integrated signal amplitudes assuming coherent vs. incoherent scattering at bedrock. Fraction of power scattered incoherently is plotted horizontally.

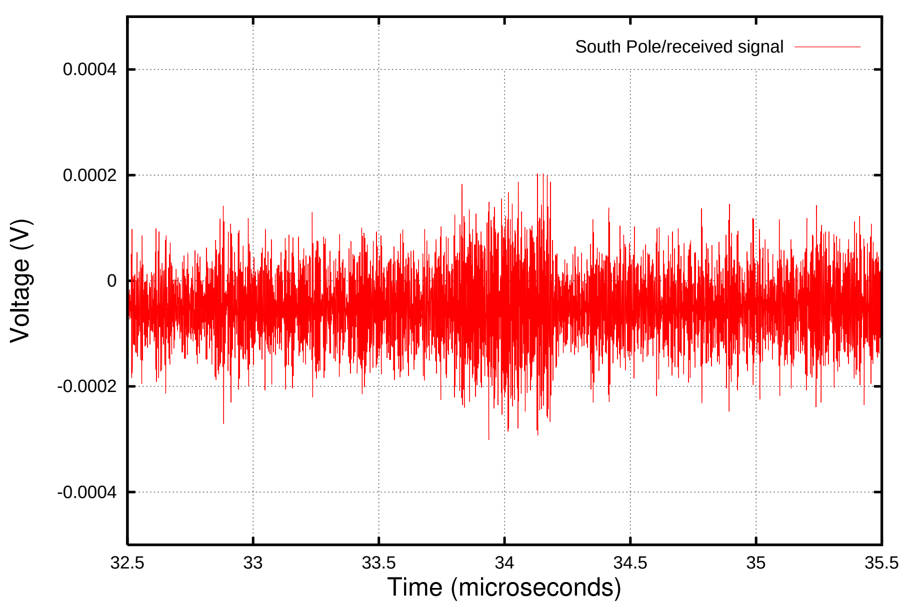

FIG. 18: Time domain (V(t)) signal observed in bottom reflection measurement at South Pole, January 2004.

and Rx signal polarization axes aligned parallel with each other, or "cross-pol", for which the receiver axis (only) was rotated by 90 degrees on the surface, these data cannot be used to extract birefringence results, discussed later in this document.) The reflection from a monochromatic 320 MHz, 400 ns long 'tone' signal emitted from a TEM horn transmitter, then later registered in a surface horn receiver (Figure 18) is observed to be approximately 400 ns in duration. A narrower input transmitter signal (40 ns) at a slightly higher frequency (380 MHz) similarly results in a correspondingly narrow received signal (Figure 19). Although not conclusive, this observation is consistent with our interpretation that the primary received reflection is of comparable duration, and has comparable spectral

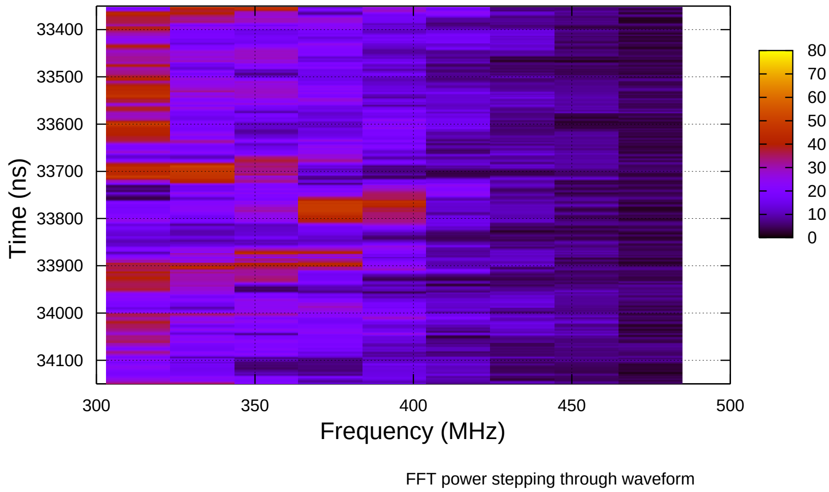

FIG. 19: 380 MHz Signal observed in bottom reflection measurement at South Pole, January 2004. Signal duration 40 ns.

content, as the broadcast signal. This indicates a coherent, specular reflection off the underlying bedrock at South Pole.

Internal Layering Effects and Volume Scattering

Layers can arise as a result of episodic events (dust or acid layers, e.g., due to volcanic eruptions[21], which result in a change in ice conductivity (and therefore ϵ'') or annual processes, including thin surface crusts which form in the summer, constituting a discontinuity in density and resulting in a contrast in the real part of the dielectric constant[22, 23, 25]. Layers of the latter type should become less important with depth as the ice approaches its asymptotic density. Anisotropies in the crystal structure of the ice may also constitute a discontinuity. Nearer to the coast, brine infiltration can also result in stratified layering. In magnitude, the ground-penetrating radar (GPR) returns from internal layers are typically 50-100 dB smaller than the returns from the bottom "echo". Precise study of layers requires extremely sensitive receivers and, in the case of annual layering, the ability to distinguish density differences of order 1-10 cm apart (<1 ns) in the ice. Interferometry or pulse modulation techniques can also be used to probe layering, provided the interferometer is sensitive to 1 ns time scales. In addition to discrete layers, quasi-continuous λ^{-4} Rayleigh scattering off air bubbles in unenclathrated ice has been considered quantitatively[23], resulting in a 'worst-case' attenuation loss estimate of $0.7\lambda^{-4}$ dB per 100 m. This extreme case corresponds to an amplitude loss of a factor of ~6, for λ_{ice} ~1 m (f_{air} ~500 MHz).

Scattering Effects in Data

Pre-signal reflections in our captured time-domain waveforms which should result from either internal layering or volume scattering are not immediately evident in our data. Comparison of the waveform in the interval 8-10 μsec from the trigger time with the interval 18-20 μsec from the trigger time shows that the rms voltage is actually slightly smaller in the former time interval than the latter, inconsistent with quasi-continuous Rayleigh scattering (Figure 20). The rms values in these plots (~100 μV) are roughly consistent with the expected thermal noise rms voltage $V_{rms} \sim \sqrt{kTBZ}$ ~20 μV, and the amplification (20 dB in power) and coaxial cable losses between the receiver and the data acquisition system.

We observe a clear modulation of the pre-reflection signal, on a timescale of several hundred ns. After digitally

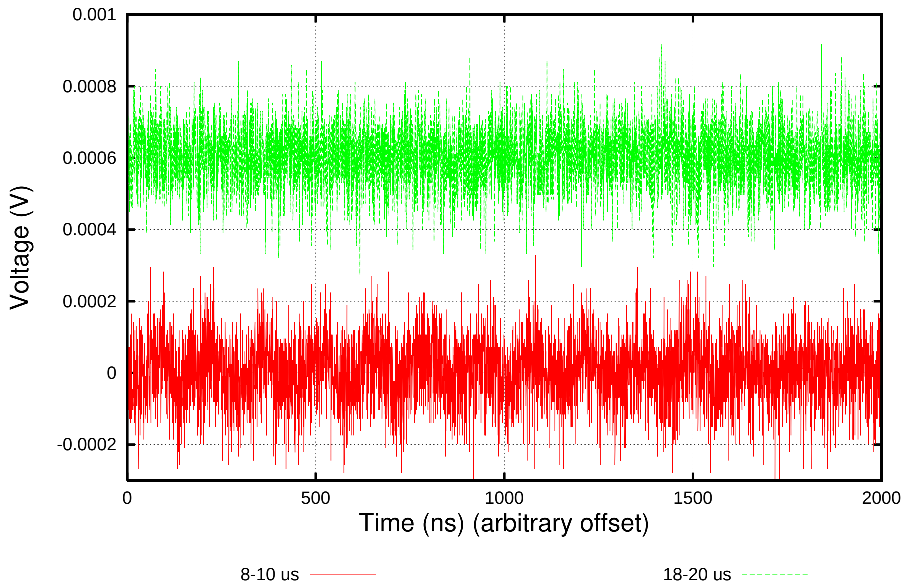

FIG. 20: Comparison of pre-reflection waveform with post-reflection waveform, no frequency filtering. Traces have been vertically offset for visual clarity.

filtering out this modulation from the Fourier transform (Figure 21), the remaining signal appears more 'thermal' in its appearance (Figure 22). The source of this apparent modulation of the pre-reflection signal is not understood,

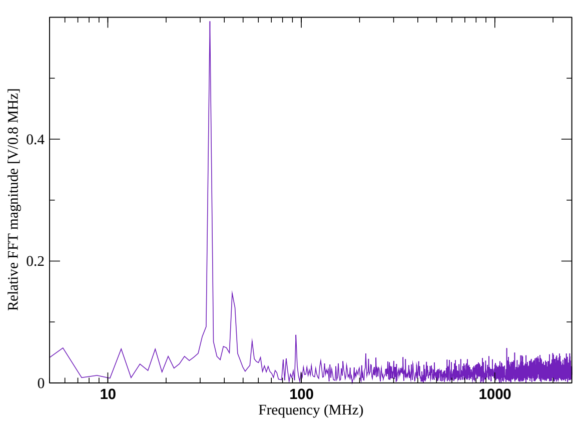

FIG. 21: V(f) of reflection signal waveform, over region prior to apparent signal reflection.

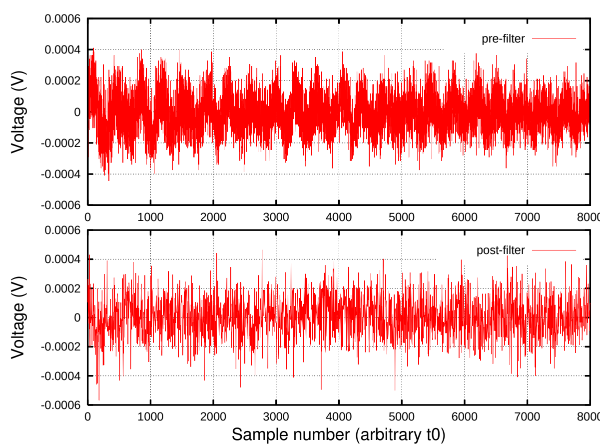

FIG. 22: Comparison of pre- vs. post-filter waveform, in region prior to apparent signal reflection.

however, we note that it does not contribute substantial power to the waveform and should therefore not substantially affect our attenuation length estimates.

Figure 23 displays the rms voltage as a function of time for the original VV configuration. We note again that the regions prior to and after the signal reflection are generally consistent with each other. All power below 32 MHz has been filtered out of this plot prior to calculation of the rms. Dividing the waveform shown in Figure 12 into 200 ns long segments beginning i) 600 ns after the apparent signal reflection, ii) at the time of the apparent

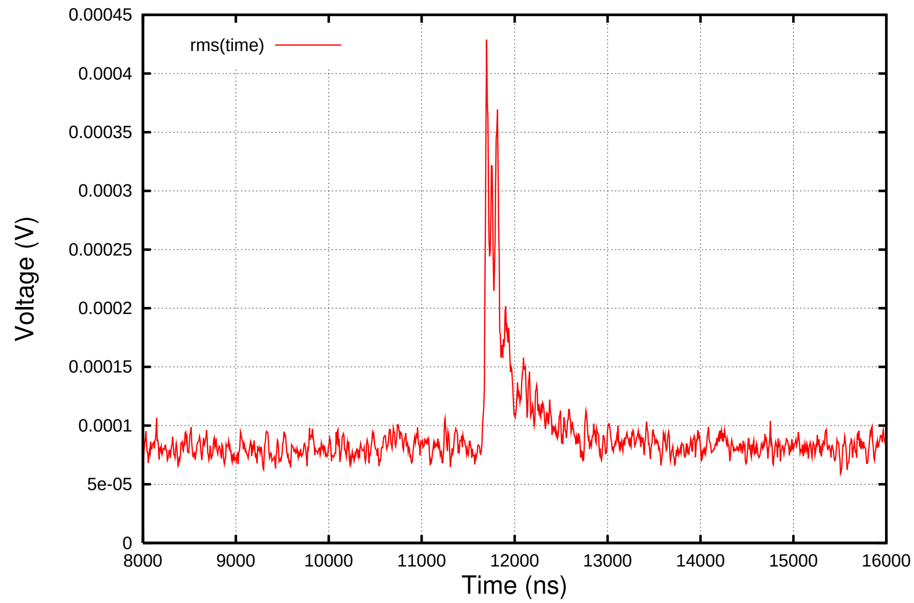

FIG. 23: rms Voltage as a function of time, original VV Tx and Rx configuration. Power below 32 MHz has been digitally removed from original V(t).

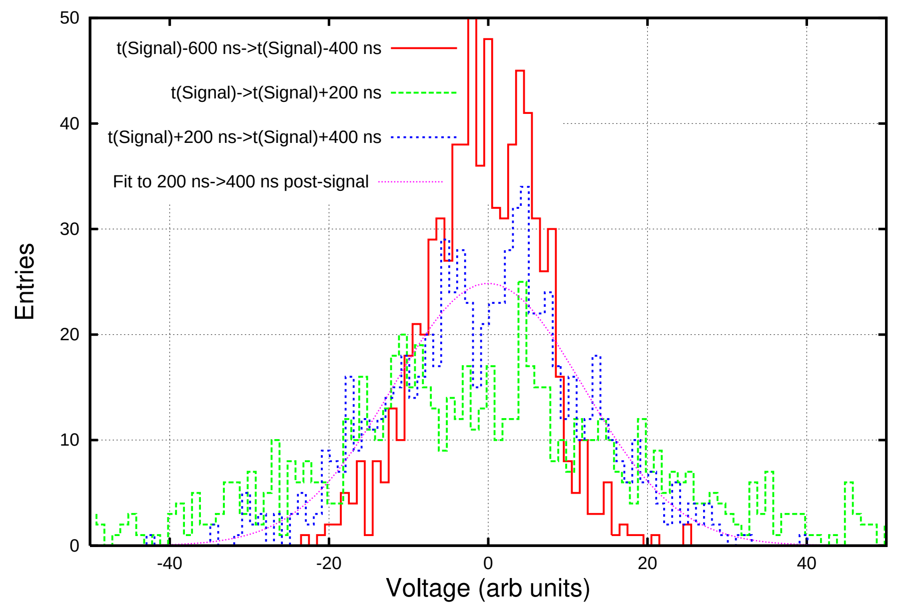

FIG. 24: Voltage distribution around the reflection signal and fit to Gaussian distribution. Presence of non-Gaussian 'tails' indicate non-thermal effects.

signal reflection, and iii) 200 ns after the apparent signal reflection, we observe that the distribution of voltages in the waveform show excursions beyond those expected for a simple Gaussian distribution, as would otherwise be expected for pure thermal noise (Figure 24).

Assumption-dependent numerical results for our pathlength-averaged attenuation length are presented in Table III. Results are presented for a variety of assumptions regarding the coherence of the signal at the bedrock, as well as the reflection coefficient at the bedrock interface.

TABLE III: Summary of attenuation length measurements, under various assumptions for the reflection coefficient and the coherence characteristics of the underlying bedrock. Values shown are averaged over multiple measurements. Errors represent statistical spread of calculated values only.

Assumed Reflection Coeff.	Signal Normalization	Assumed Basal Scattering	Integrated Reflected Signal	Calculated $\langle L_{atten} \rangle$
1.0	In-air	Coherent	10 ns	340 ± 15 m
1.0	In-air	Coherent	50 ns	351 ± 15 m
1.0	In-air	Coherent	250 ns	616 ± 32 m
1.0	In-air	Incoherent	10 ns	441 ± 25 m
1.0	In-air	Incoherent	50 ns	458 ± 26 m
1.0	In-air	Incoherent	250 ns	1055 ± 95 m
1.0	Absolute	Incoherent	250 ns	628 m
0.3	Absolute	Incoherent	250 ns	1051 m

In principle, one might argue that one should properly include the cross-polarization (i.e., HV or VH) signals into the tabulation of the received signal. Reciprocity suggests that, if a purely V-transmitted signal can excite the H-terminals of the receiver horn antenna, excitation of the V-terminals of the transmitter can also result in excitation of the H-terminals of the transmitter. In that case some of the H-received signal is simply the transmission of this H-component, which has preserved its polarization in its traversal of the intervening ice. We therefore only include signal from that polarization component corresponding to that originally transmitted. Including the cross-polarization signal would increase the estimated attenuation length by ∼10%.

Attenuation length dependence on temperature profile

Radiofrequency absorption is a strong function of temperature. Figure 25 displays our measurements of temperature as a function of depth at our borehole site, overlaid with two possible extrapolations in the region below our last temperature measurement at a depth of 100 meters. We estimate an uncertainty of approximately 0.2 degrees Celsius in each of our measurement points. Given our measured average attenuation length $\langle L_{atten} \rangle$, in order to extract a numerical estimate of the attenuation length as a function of depth we must extrapolate the temperature at a depth of 97 m to the temperature at the bedrock. To our knowledge, a full temperature profile down to bedrock at our site is not currently available. In the absence of a dedicated scan of the frequency dependence of the received signal, we assume flat response of the transmitter and receiver between 200 MHz and 1000 MHz, ignore any frequency dependence of L_{atten}, and weight the received signal amplitude by λ to include the expected effective height dependence of the transmitter and receiver antennas. Using bedrock reflectivity equal to unity, and an average attenuation length of 450 m, a parabolic extrapolation of temperature down to a warm bed gives an implied attenuation length at -50 C and 380 MHz of 1480 m, within 2% of the central value obtained at South Pole[2]. A flat extrapolation at constant temperature gives a value only half as large.

S_{12}(ice) measurements - signal arrival time considerations

Birefringence considerations

In principle, ground-penetrating radar can be used to probe birefringent asymmetries, for both the real and imaginary pieces of the dielectric constant. A continuous wave (CW) network analyzer signal, fed into a Transverse ElectroMagnetic (TEM) horn, can be used to excite one particular polarization. In the case where that signal polarization axis coincides with one of the linear birefringence axes (aka "optical axes", or "ordinary" and "extraordinary" axes), no birefringent asymmetry is observed. In the case where the signal polarization axis projects onto two orthogonal birefringence axes, a birefringent asymmetry ($\delta_{\epsilon'} \neq 0$) in the real part of the dielectric constant will result in interference between the two orthogonal signals arriving at the receiver, with some frequency and pathlength-dependent reduction in observed signal magnitude. In the case where the signal polarization is at 45 degrees relative to the birefringent axes, each of the equal-amplitude HH and VV projections would display a reduced amplitude over

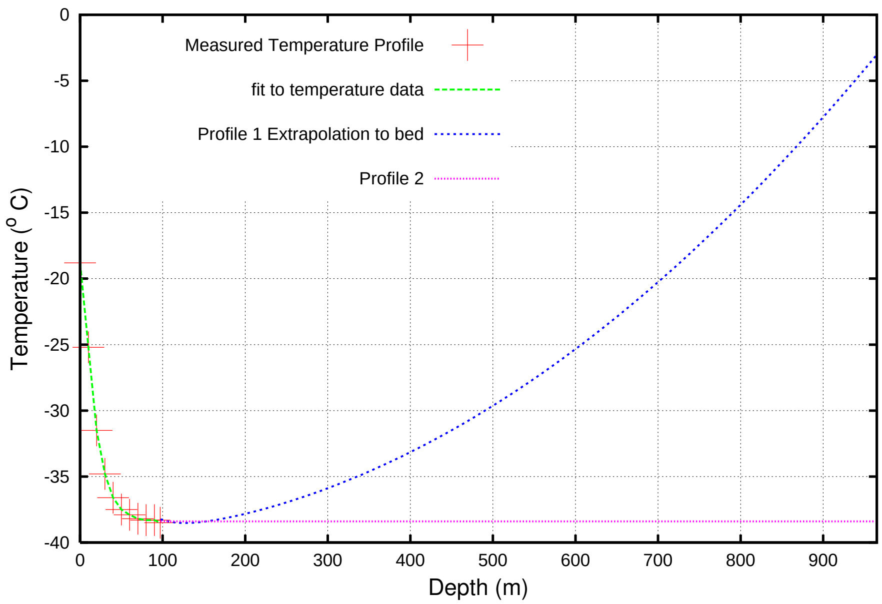

FIG. 25: Measured temperature profile at borehole site. Also shown are temperature profiles considered for systematic uncertainty estimate in extracted attenuation length. We note that all measurements (to our knowledge) indicate a warming of ice to near 0° C at the bedrock; "Profile 2" is therefore considered to be an extremely unlikely, and overly pessimistic case.

the time when only one projection is being measured, followed by an interference pattern with amplitude varying from zero to the maximum observed for the unrotated orientation, over the timespan when the signals propagating along the birefringent axes interfere at the receiver antenna, again followed by a reduced-amplitude post-interference single-polarization signal. Note that this gives us one criterion for the antenna orientation which best matches the birefringent axes – in that configuration, the observed time duration of the signal is minimized and the observed peak amplitude is maximized.

Considerable literature and experimentation have been devoted to ice birefringence. Some of the relevant measurements thus far are summarized in Table IV. Here we restrict ourselves to only the most recent experimental efforts in Antarctica. Frequency-domain experiments typically measure the power reflected off the bedrock as a function of orientation angle of transmitter and receiver. Variations in the power are typically the combined result of anisotropies in bedrock scattering and also birefringence. Multiple measurements at a variety of orientation angles and frequencies allow one to separate, to a large extent, the two contributions. Data collected on Brunt Ice Shelf near Halley Station resulted in an estimate of the minimum birefringent asymmetry in the effective permittivity ($\delta_{\epsilon'}$) of 0.14–0.52%[11], depending on location. The same experimental apparatus employed at George VI Ice Shelf yielded values typically 3× smaller.

Continuous wave data taken using horn antennas rotated in the horizontal plane and broadcasting along the axis perpendicular to the bed ("c-axis") over a 300-km traverse from Dome Fuji show a very clear sinusoidal pattern, with an amplitude modulation ≈80% over π radians[9]. This is interpreted as direct observation of birefringence due to the asymmetry in the crystal orientation fabric ("COF"), caused by the ice flow itself along the gravitational gradient and resulting in crystal orientation perpendicular to the flow direction[24]. Schematically, the geometry of the crystal orientation, relative to the putative birefringence axes, is shown in Figure 26.

Direct measurements of Vostok ice cores, however, indicate no preferred ice crystal orientation over the first 400 meters in depth, followed by a mixture of COF both parallel to, as well as perpendicular to the c-axis (i.e., along the vertical, or $\hat{z}$ and along an axis perpendicular to the horizontal ice-air interface) over the next 1400 m. Below that value, the COF is found to align along the c-axis, with crystals preferentially stretched along the vertical. We note also that measurements thus far indicate that sheet ice has a uniform density below ∼200 m, so any alignment of the internal fabric evidently does not result in any bulk change in the crystal packing.

As an alternative to frequency-domain measurements, one can directly measure asymmetries in the time domain using a pulsed signal. This approach has the disadvantage of obscuring the frequency dependence of the signal propagation, but the advantage of isolating through-air signal leakage due to the side lobes of a typical horn beam

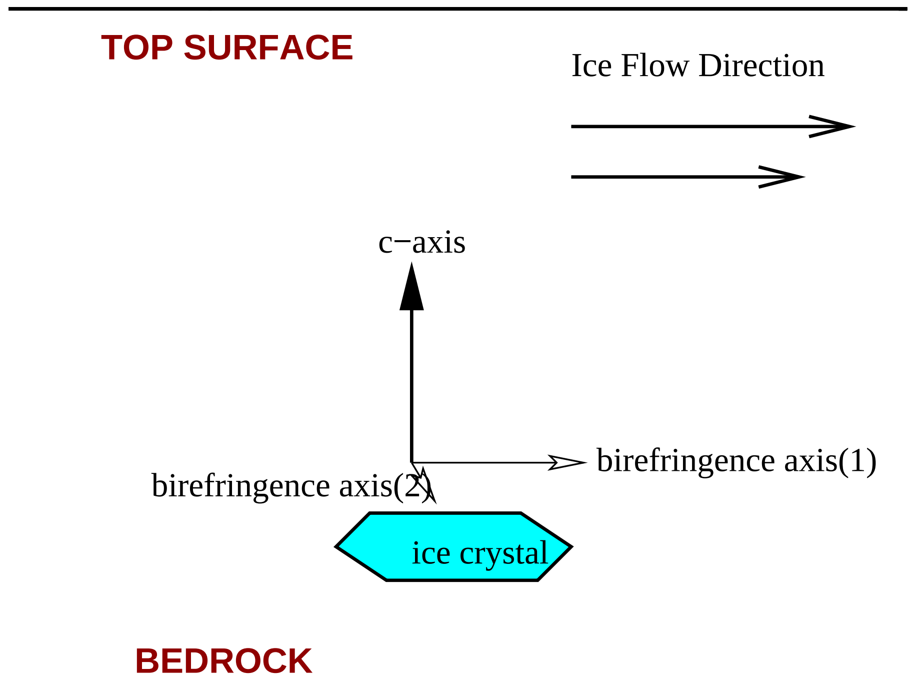

FIG. 26: Presumed orientation of birefringence axes, relative to ice flow.

TABLE IV: Summary of birefringence measurements to date.

Group	Locale	$\delta_{\epsilon'}$ Result	Comment
Matsuoka *et. al.* (1997)[26]	Lab Ice	∼3.4%	39 GHz
Fujita & Mae (1993)[29]	Lab Ice	∼1.1%	
Doake, Corr, Jenkins (2002)[11]	Brunt Ice Shelf	>0.14–0.47%	
Doake, Corr, Jenkins (2002)[12]	George VI Ice Shelf	>0.05–0.15%	
Woodruff & Doake (1979)[13]	Bach Ice Shelf	0.52%	
Fujita *et. al.* (2003)[14]	Mizuho Station	measurable	
Fujita *et. al.* (2006)[30]	Dome Fuji	0.05%	>500 m, multi-parameter fit
Fujita *et. al.* (2006)[30]	Mizuho	1.5%-3.5%	<500 m, multi-parameter fit

pattern and/or other possible multi-path effects. In this case, $\delta_{\epsilon'} > 0$ results in a measurable time difference between two signal polarizations; $\delta_{\epsilon''} > 0$ results in an amplitude difference between two polarizations.

Experimental Comparison of Bottom Reflection signals

Bottom reflection data were taken in "VV", "HH", and "VH" orientations. The start times (t_0) from the pulser for our measurements are found to be identical to within ∼200 ps. Figure 27 compares the trigger crossing time for the "VV" and "HH" orientations.

Comparing "HH" to "VV" reflections, we observe that the echo time recorded for the "HH" signal is advanced by 15 ns relative to the "VV" echo signal time (Figure 28, and zoomed in Figure 29). Aside from the unlikely possibility that the bottom surface has local 'patches' which favor different polarizations, it would appear that the most likely explanation for this observed time difference is due to wavespeed differences along two axes. Interpreted as birefringence, the implied asymmetry is approximately 0.12%. Although not fully probed owing to time and cable length limitations, and also problems with data acquisition waveform capture (the voltage resolution setting on the digital oscilloscope was, unfortunately, unusably coarse), we note that:

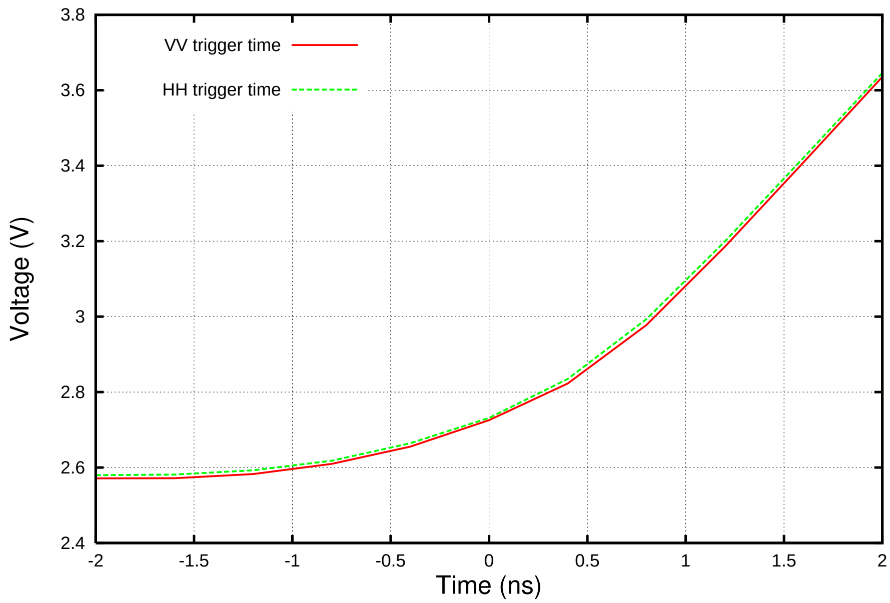

FIG. 27: Comparison of trigger time for bottom reflection measurements for HH vs. VV orientations (60 event average). Trigger threshold is set to 2.72 V. Time difference in t_0 between HH vs. VV measurements is insignificant compared to time delay measured between received signals.

- the magnitude of the HH vs. VV signals were relatively constant when the receiver antenna was displaced along the N-S axis by approximately 170 m (in that case, the illuminated reflecting area of bedrock should be displaced by ∼85 m) and then rotated in 22.5 degree steps over 180 degrees. The intent here was to probe the specular component of the surface scattering and attempt to discern variations in peak receiver voltage, as a function of orientation. The measured values of peak receiver voltage, read off the TDS694C oscilloscope screen, are presented in Figure 30. We observe from Figure 30 that: a) our initial "VV" orientation of –14.8 degrees seems to be close to the maximum voltage orientation; b) from interference effects, and assuming that the birefringent asymmetry in the real part of the dielectric constant is substantially larger than in the imaginary component, we would naively expect maxima at intervals of $\pi/2$, corresponding to those orientations for which the antenna polarization axis is aligned with either of the optical axes; c) absent physical effects which rotate the polarization plane of the propagating signal, we would expect the received cross-polarization ($V \to H$, e.g.) fraction of the received signal to be approximately constant. The largeness of the point-to-point systematic errors and the lack of comprehensive data notwithstanding, such constancy is not obviously observed. Rather, there appears to be an anti-correlation between "co-pol" (VV or HH) signal strength and cross-pol (VH) signal strength – when the former is largest, the latter is smallest, and vice versa.
- To check antenna systematics, the surface horn transmitter and surface horn receiver were rotated in the horizontal plane by –90 degrees; in that configuration, we find HH(rotated)=VV(unrotated), and VV(rotated)=HH(unrotated). This indicates that the observed time-domain asymmetry is not an artifact of antenna effects.

Figure 31 displays the received signals for both the original VV and HH orientations, the signal observed when the surface antennas are each rotated by –45 degrees ($\pi/4$), and the vector sum of the VV and HH signals. The latter is obtained by projecting the VV and HH data onto an axis bisecting VV- and HH-, and adding the projected components. Neglecting thermal noise contributions, which would add a random voltage with rms $V^{rms}_{thermal\ noise}$ point-to-point, our VV+HH sum model should coincide with the –45 degree data. This comparison is, unfortunately, inconclusive.

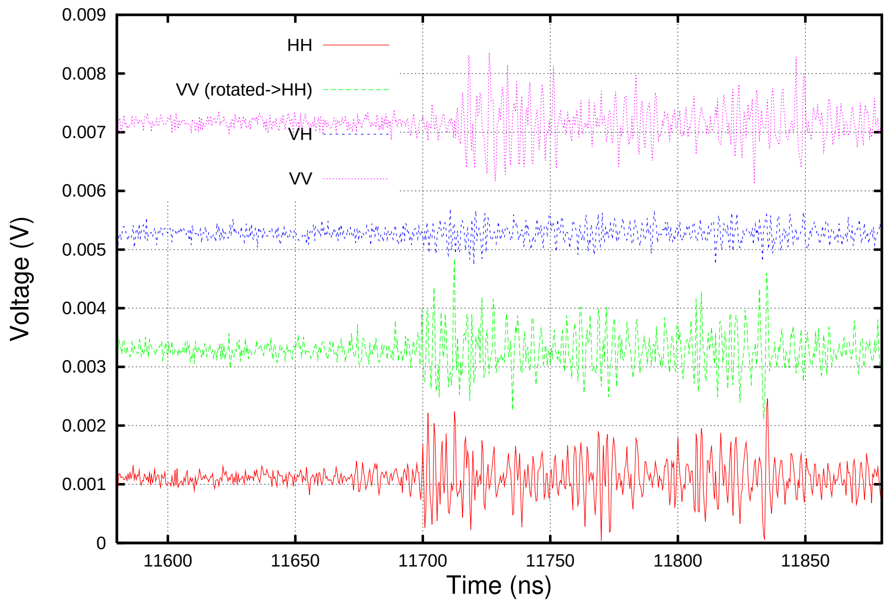

FIG. 28: Received signal as a function of time for indicated orientations. "VV→HH rotate" refers to the Tx and Rx orientation for which the VV axes of both Tx and Rx have been rotated into the initial HH orientation. In this (and successive) Figures, the three uppermost signals have been vertically offset to enhance visual clarity.

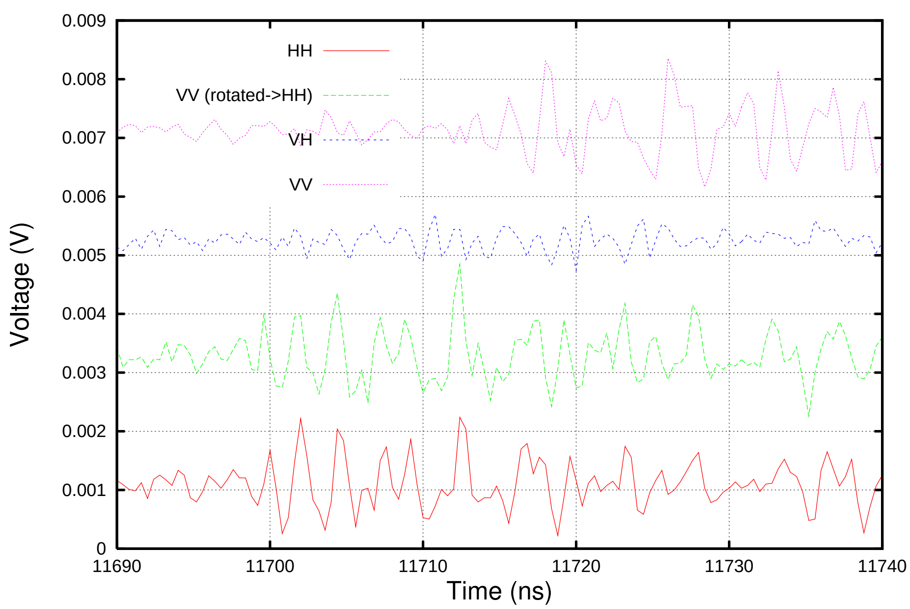

FIG. 29: Zoom of previous Figure.

Cross-Correlation Analysis

A cross-correlation analysis can also be used to both extract the signal hit-time, and also assess the degree of 'similarity' of the recorded waveforms. In this analysis, a 200 ns-long segment of the waveform, centered on one of the reflection signals observed in the initial VV-orientation, comprises the 'filter' pattern. The 'VV→HH rotated', HH and HV waveforms comprise 'templates'. Over a 4000 ns template segment, centered on the observed bottom

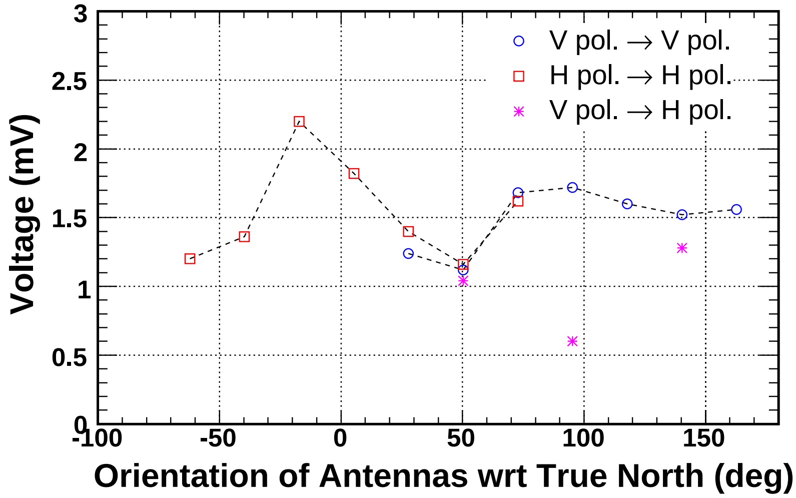

FIG. 30: Maximum measured bottom reflection voltage (as read directly from oscilloscope) with surface receiver horn displaced 170 m south of initial measurements. Typical measurement uncertainty is estimated to be of order 20% at each point. "Negative" corresponds to a clockwise rotation from true North; i.e., in the direction towards East.

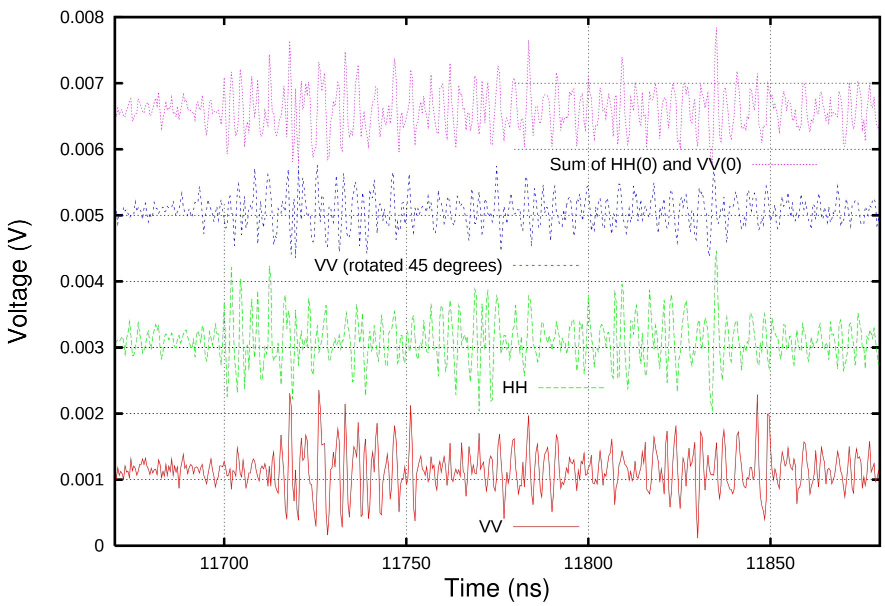

FIG. 31: Vector sum of HH and VV signals (our birefringence model, top) compared with data received signals, as indicated. Plots have been vertically offset for visual clarity. In the context of our model, the top plot should correspond to the second-from top plot ("VV (rotated 45 degrees)").

reflection in each of the template waveforms, we calculate the correlation parameter $\mathcal{C} = \Sigma_{i'=0}^{3800}\Sigma_{i=0}^{200} V_{i,filter} V_{i',template}$. Figure 32 illustrates the similarity in the HH and VV waveforms, which have nearly identical cross-correlation maximum amplitudes.

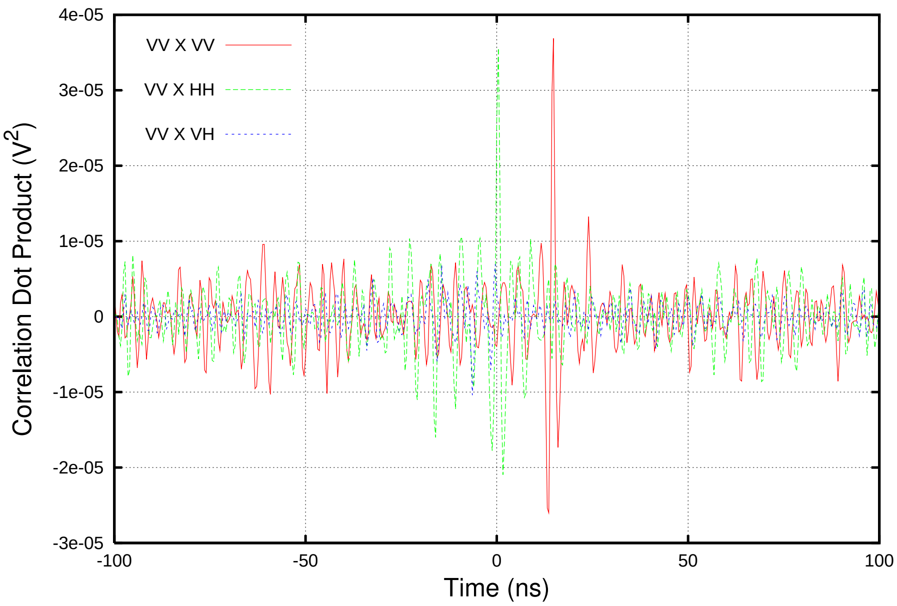

FIG. 32: Cross-correlation parameter, as described in text.

Faraday Rotation

An apparent propagation asymmetry can also be due to the interaction of an electromagnetic wave with an external magnetic field (Faraday rotation). The interaction of electromagnetic radiation having a propagation wave vector ($\vec{k}-$) parallel to an external magnetic field $\vec{B}$ can lead to an apparent rotation of the electric field polarization plane. This can be visualized as a decomposition of the planar wave into left- and right-circular polarization components, which interact differently with the ambient field and propagate at different velocities. In that sense, Faraday rotation can be thought of as birefringence of circular, rather than linearly polarized basis states. The degree of angular rotation β over a distance d is specified by the Verdet constant (given by $\mathcal{V} = -(e\lambda/2mc)dn/d\lambda$) via $\beta = \mathcal{V}Bd$. For water at 20° C, the measured value of $\mathcal{V}$ is 0.00038 rad/m/Gauss at optical wavelengths, where it has been studied most extensively. Although the value of the local magnetic field was not measured at our particular site, the proximity to the South Magnetic Pole (defined as the point where the geomagnetic field is vertical) at 65°S and 139°E implies that the magnetic field is largely aligned along the $\hat{z}$, or vertical (c-axis). Using Verdet constant data for water (this may not be directly applicable to ice, however, ice data were not available) and a value for the earth's field of 1 Gauss leads to an expected rotation of θ_{FR} ~20 degrees over the one-way path from surface to bedrock. Since the underlying bedrock has a larger index-of-refraction than the ice sheet above it, the electric field vector is expected to invert (i.e., rotate by 180 degrees around $\vec{k}-$) upon reflection, after which the electric field vector rotates in the opposite sense, as viewed from behind. The two effects add, so that the total rotation, relative to the sent signal, will be $\theta_{tot} = 2\theta_{FR} + \pi$, and could therefore affect the measured leakage into the 'cross-polarized' signal. However, Faraday rotation is not expected to give a net time stagger between the two measured linear polarizations.

Broadcast through firn

Our measurement of the birefringent asymmetry is, of course, only the asymmetry projected onto the vertical signal propagation axis. To probe possible asymmetries in the horizontal plane (and also surface transmission effects), narrow pulses were broadcast from the discone antenna buried at a depth of 97 m into the ice, and the signal measured in a surface horn receiver antenna. Due to the small calibre of the borehole, only a vertically polarized antenna (dipole or discone) with a large vertical:horizontal aspect ratio could be used as a buried transmitter. Figure 33 displays the Vertical-polarization and Horizontal-polarization signals received by the surface horn when broadcasting from the in-ice, vertically-oriented discone. The observed Hpol signal is consistent with the known

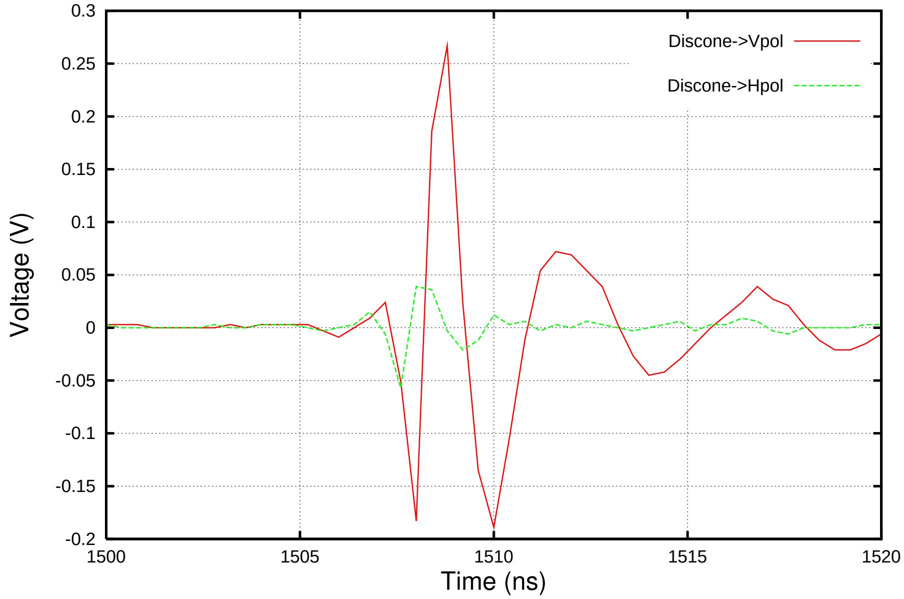

FIG. 33: Comparison of typical Vpol signals measured by surface horn receiver from in-ice discone antenna.

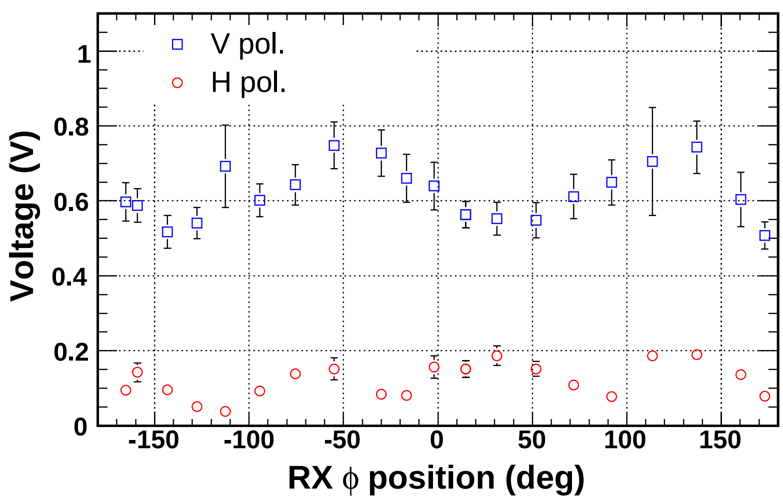

FIG. 34: Received surface horn signal strength, broadcasting from in-ice discone, as a function of azimuthal angle.

cross-talk and isolation between the vertical and horizontal polarizations of the surface horn receiver. Given the short in-ice pathlength, and cross-talk complications, it is somewhat difficult to interpret the equality of the observed signal times in terms of birefringence. Moreover, since most of the signal path is through the firn, it is quite possible that the ice crystal fabric has not yet, at this limited depth, established a preferred orientation. Taken at face value, the observed asymmetry of 0.12% in our S_{12}(ice) measurements would imply a difference in the Hpol vs. Vpol signal arrival times of about 700 ps, just at the edge of our sensitivity.

The peak received signal strength (corrected for the distance from discone to receiver) shows a clear sinusoidal dependence, as a function of azimuth, as shown in Figure 34. We have investigated the possibility that the observed azimuthal signal strength dependence might be a simple consequence of the intrinsic beam pattern of the discone

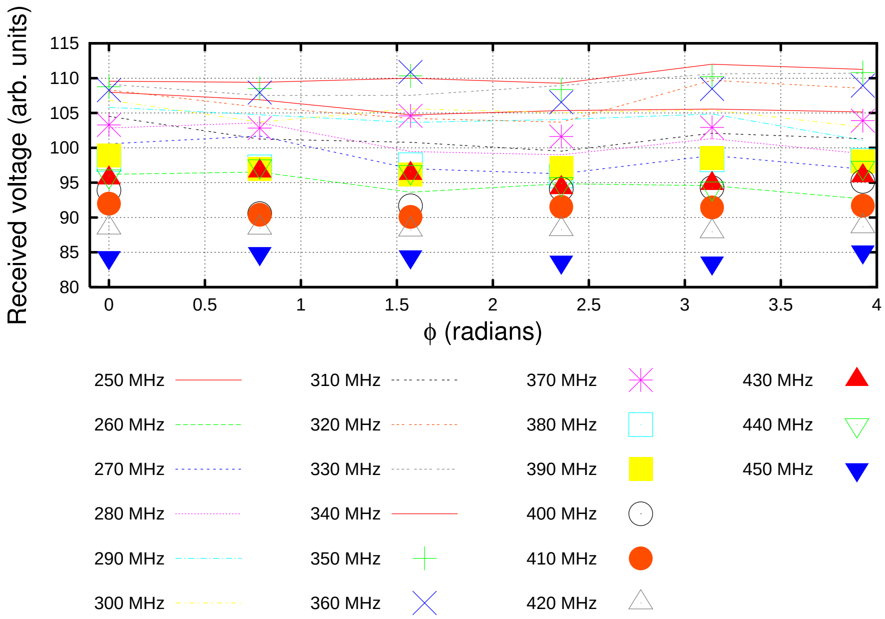

FIG. 35: Received azimuthal power, broadcasting with discone (in-air) to surface Seavey horn, as a function of frequency.

itself. A second discone, similar in construction to the in-ice discone (the original discone was left in the ice for the primary ANITA mission) was rotated azimuthally in-air at an elevation of $\sim$2 m and the signal strength measured in the surface receiver horn (Figure 35). The lack of azimuthal variation observed over π radians indicates that the structure observed when broadcasting from the in-ice discone to the surface receiver is not a consequence of the discone beam pattern. The fact that the received signal magnitude seems correlated with the local surface gradient suggests that the observed variation may be due to the polar angle dependence of the signal emission and reception. In that case, however, we expect a 2π rather than a 4π modulation of the observed receiver signal.

Nevertheless, exit angle dependences were explicitly investigated. By default, the receiver horn antenna was oriented with an inclination angle of -11 ± 1.5 degrees relative to the horizon (i.e., pointing down relative to true horizontal). The local surface elevation gradient resulted in a measured maximum difference in snow exit angle of amplitude 4 degrees. To investigate the polar angle dependence, the receiver signal was measured as a function of cant angle with respect to the horizontal (Figure 36). The magnitude of the observed variation indicates that no more than $\sim$10% of the observed azimuthal variation might be due to local exit angle effects.

Surface Roughness Effects

The observed variation may also be the result of surface roughness effects. We have measured the rms variation of the local snow elevation, and the dependence of the observed signal strength on variations in surface roughness. At a radial distance of r=70 m from the borehole, the received signal strength was measured initially, then the snow surface was 'roughed' with a shovel. Next, a shallow trench ($\sim$25 cm deep) was dug and 'roughed' again and the signal strength re-measured. Figure 37 shows the results of this procedure. Table V shows the average value of snow 'depth' and also the rms-variation in the snow depth, sampled randomly in the 2m x 2m patch of snow surface directly in front of the antenna. Given the fact that the surface roughness was considerably larger than that expected 'naturally', we assess the systematic uncertainty in ANITA signal reception due to surface roughness effects, based on our measurements alone, as $\sim$10%. It should be mentioned that we have conducted our measurements only over an extremely limited area compared to the variety of surface features actually probed by ANITA and this estimate is not necessarily applicable to the entire continent.

As an additional measure of surface roughness effects, the transmitted discone signal was measured by the surface horn receiver along a constant azimuth, and also with the surface horn at the same value of radial distance but displaced in azimuth by approximately 1 m to the West, corresponding to the spatial scale of the surface illuminated region. This displacement is sufficiently small that there should be no significant change in received voltage due to

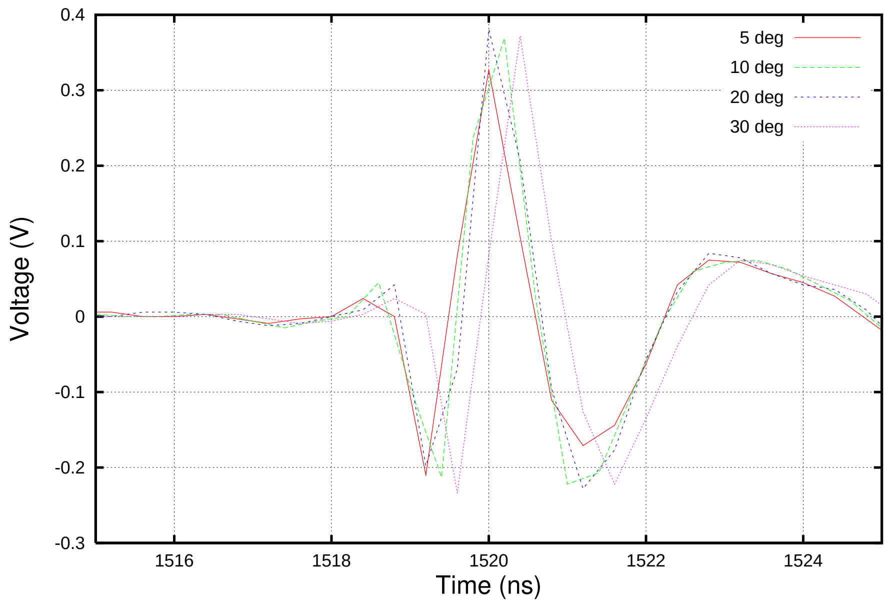

FIG. 36: Signal dependence (broadcasting from in-ice discone) on surface horn receiver cant angle; r=70 m.

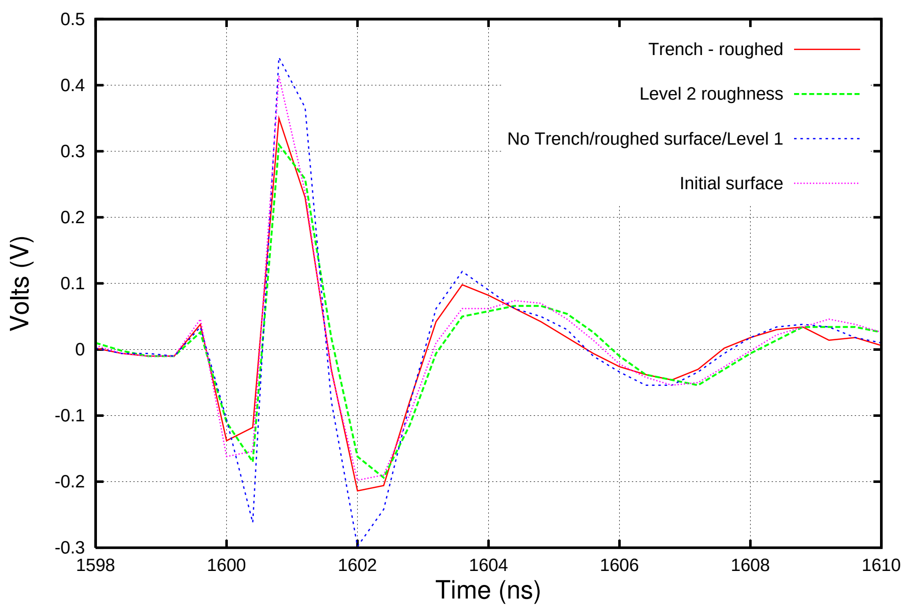

FIG. 37: Comparison of signals received for differing amounts of (artificially created) surface roughness in the region in front of the surface horn. For all these measurements, the surface receiver horn is elevated approximately 0.5 m, so that the center of the antenna is elevated approximately 1 m above the surface.

beam pattern uncertainties; we attribute any observed variation to the different air-ice interfaces probed from the two receive points. In this case, we again observe $\sim$10% variation in received signal amplitude. Figure 38 shows the signal strength as a function of radial distance from the borehole, along two slightly different lines in azimuth. The degree of scatter, for points very nearby in ϕ provides a measure of what we have not only attributed to 'surface roughness' systematic error, but also the single-shot measurement error.

TABLE V: Summary of direct measurements of snow surface depth variation. d=0 corresponds to the estimated average surface level of the surrounding snow. r is the radial distance between the surface horn receiver and the in-ice discone, $\bar{d}$ gives the average of the measured snow depth values, and σ_d is the rms of the measured depth values.

r	Samples	Surface condition	$\bar{d}$	σ_d
71 m	26	1^{st}-level roughness	27.15 cm	7.2 cm
71 m	31	2^{nd}-level roughness	30.5 cm	7.9 cm
71 m	27	in-trench	34.6 cm	6.7 cm

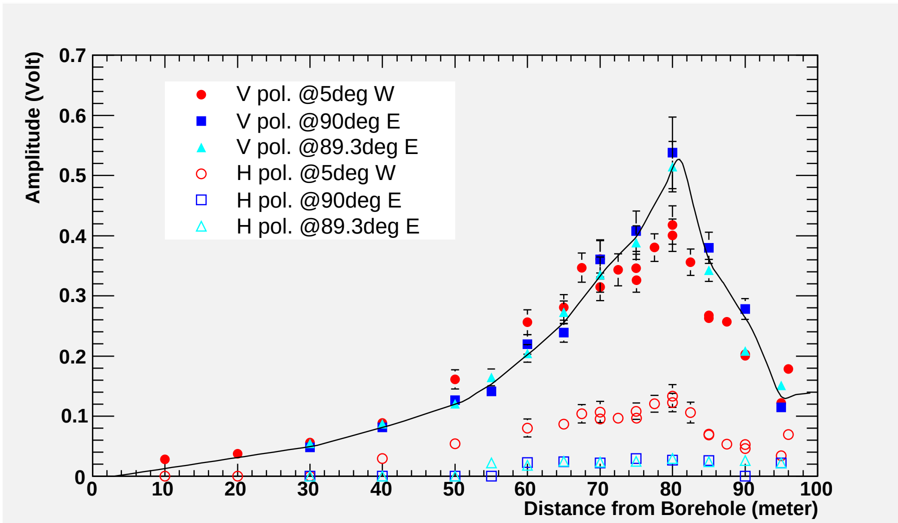

FIG. 38: Measured peak voltage in surface receiver horn (in-ice discone transmission) along three lines in azimuth, two of which are close to each other. Since the discone broadcasts over all polar angles, there is always a ray connecting the in-ice discone to the above-ice surface horn receiver.

Amplitude dependence on density profile

In addition to the known discone and receiver horn beam patterns, and the separation between them, the signal amplitude at the surface receiver horn is primarily dependent on the Fresnel coefficient at the ice-air interface. The incident scattering angle as the ray emerges into the air therefore depends on the density profile $\rho(z)$, which determines the ray tracing through the firn. In Figure 40, we show the result of a simulation based on two test firn density profiles (Figure 39, showing only the first 100 meters of depth near Taylor Dome, from Figure 10, as well as the fit using South Pole density measurement data overlaid). These amplitude data slightly favor the South Pole density profile as a better indicator of the correct firn density.

Signal arrival time dependence on density profile.

In principle, the discone→surface receiver signal arrival time data can also be used to directly verify the density profile over the first 100 m of ice, as done previously at the South Pole[27]. Figure 41 shows the signals received as the discone was lowered, at approximately 10 m intervals into the borehole. Table VI gives the signal arrival time and amplitude characteristics (due to operator error, the maximum possible measured voltage was only 0.1 V). Assuming the index-of-refraction is related to density via the Schytt model[28] ($n(z) = 1. + 0.86\rho(z)$), we find reasonably good agreement between our tabulated results and the data taken from Taylor Dome itself. For comparison, we have also included the expected times using the $\rho(z)$ profile using density data from the South Pole. Our propagation time measurements suggest that the density profile at our experimental site is slightly less sharp than the density profile obtained at Taylor Dome itself. Figure 42 presents our results graphically. In this case, rather than taking the "zero" hit time as the time recorded when the discone was at a depth of 10 meters, we compare our measurements

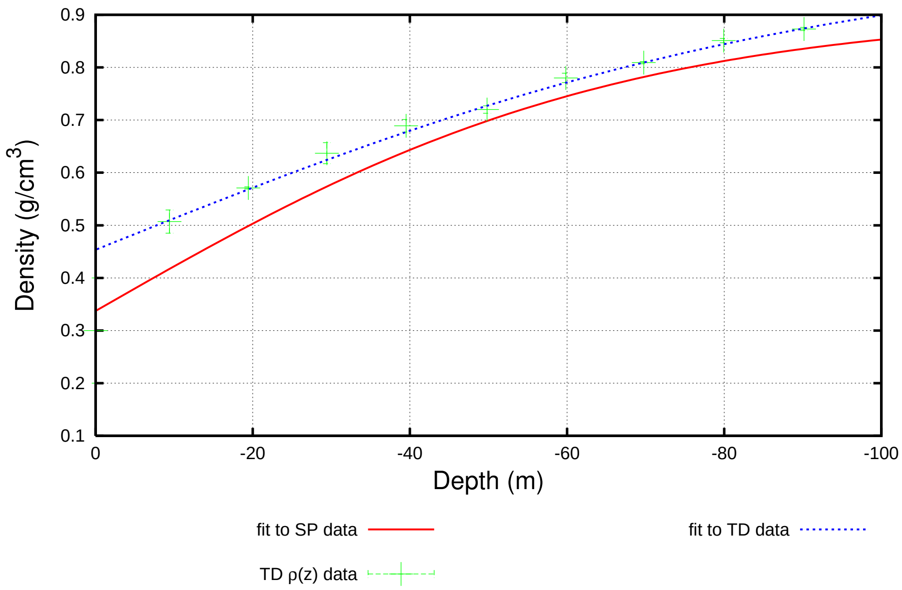

FIG. 39: Taylor Dome density data (Fitzpatrick, 1994, and Dixon, 2007) points and fit to density profile, compared with fit to density profile data at South Pole. These profiles are used to calculate the expected propagation between the in-ice discone and the surface receiver.

Depth	Recorded Signal time (ns)	Peak Voltage (V)	TD $\rho(z)$ fit time (ns)	SP $\rho(z)$ fit time (ns)
+1.1 m	1146	0.040		
0 m	1145	0.010		
–10 m	1178	0.009	1178	1178
–20 m	1213	0.020	1213.7	1210.6
–30 m	1251	0.024	1251.8	1246.3
–40 m	1292	0.040	1291.8	1284.7
–50 m	1332	0.064	1333.7	1325.4
–60 m	1374	0.071	1377.3	1368.1
–70 m	1420	≥0.1	1422.4	1412.2
–80 m	1466	≥0.1	1468.8	1458.5
–90 m	1513	≥0.1	1517.6	1506.2
–97 m	1547	≥0.1	1551.9	1540.0

TABLE VI: Comparison of measured signal arrival time, as a function of depth, with signal arrival time predicted using the Taylor Dome density profile used herein, and also the measured South Pole density profile through the firn. Indicated times include cable propagation times, in addition to transit times through ice/air.

to the 100 meter depth propagation time data.

Conclusions

Our initial goal was to measure the attenuation length of ice at a site close to the Antarctic coast (Taylor Dome) and to compare that value with previous measurements at South Pole. This is one of a series of anticipated experiments to map out ice properties over the large area probed by the balloon-borne ANITA neutrino detection experiment. Using a variety of somewhat redundant measurements, we estimate the uncertainty in the expected ANITA signal strength due to uncertainties in transmission across the air/ice interface to be of order 10%.

We observe a clear signal, reflected off of the underlying bedrock. Determination of the exact signal strength

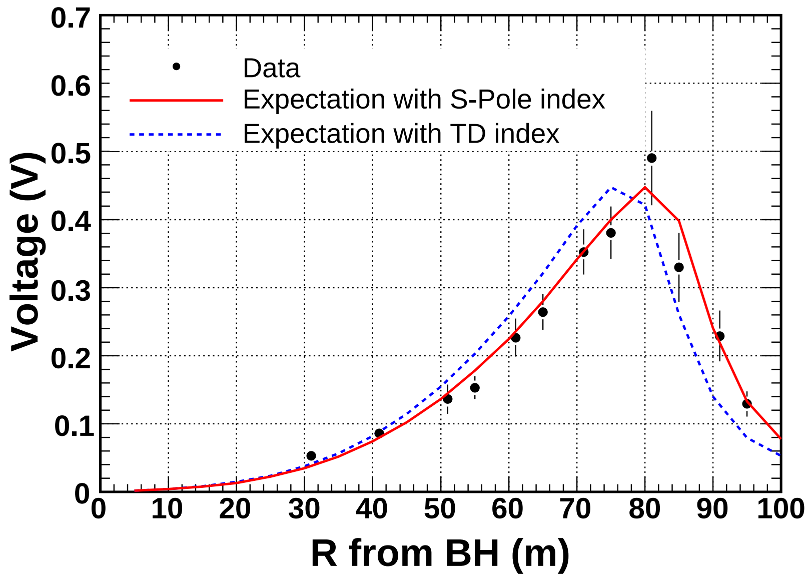

FIG. 40: Average of 90° and 0° measured peak voltages in surface receiver horn (in-ice discone transmission) with fit to expected amplitude, as a function of radius.

for this bottom reflection is complicated by uncertainties regarding the bottom topography and the bedrock-ice reflection coefficient, as well as possible interference effects. For a variety of orientations, with both Rx and Tx identically polarized, and probing a variety of surface Tx/Rx locations over a 100-meter surface radius region, we measure peak reflected voltage values that are consistent to within approximately 30%, with a S:N of ~4.0, implying attenuation lengths roughly consistent with measurements made at the South Pole. Additionally, we find strong evidence for an asymmetry in the real part of the ice dielectric constant, which we interpret as the first observation of time-domain birefringence.

Due to the reduced maximum amplitude, the efficiency for registration of ultra-high energy neutrinos, based on a voltage threshold-crossing event trigger, may be reduced if the birefringent asymmetry is 0.12% and the result of crystal orientation fabric (COF) alignment. The quantitative impact of any possible birefringence will depend on the experimental details of a given data acquisition system and the location-specific ice properties. Using a Monte Carlo simulation for the RICE[3] experiment at the South Pole, consisting of 16 vertically-oriented dipoles confined to a 200 m x 200 m x 200 m cube centered 200 m below the surface at the South Pole, we estimate a loss of ~15% in effective neutrino detection volume, roughly independent of neutrino energy. For the ANITA experiment, the effect is expected to be considerably smaller, since the data acquisition system integrates ~8 ns after the initial trigger signal, and also since almost all the detected neutrino flux corresponds to the case where the Cherenkov electric-field vector is polarized predominantly in the vertical plane, whereas birefringence should be most noticeable for the case where the $\vec{E}$ polarization vector coincides with one of the principal axes of the ice crystal (assumed to be oriented horizontally, in the case where the fabric is defined by the horizontal ice flow). Additionally, the bulk of the sensitive volume probed by ANITA is slower-moving, thicker interior ice, for which birefringent effects are expected to be somewhat smaller than near the continental periphery.

A suite of additional measurements at a variety of icecap locations, perhaps in association with future traverses, are needed to fully map out ice properties across the continent. In principle, the extensive measurements conducted to determine the Antarctic and Greenland ice thicknesses can also be searched for time delays as a function of transmitter/receiver orientation. Those studies are currently underway. Particularly important is the determination of dielectric properties measured in the vertical plane, for which there is thus far somewhat less *in situ* data.

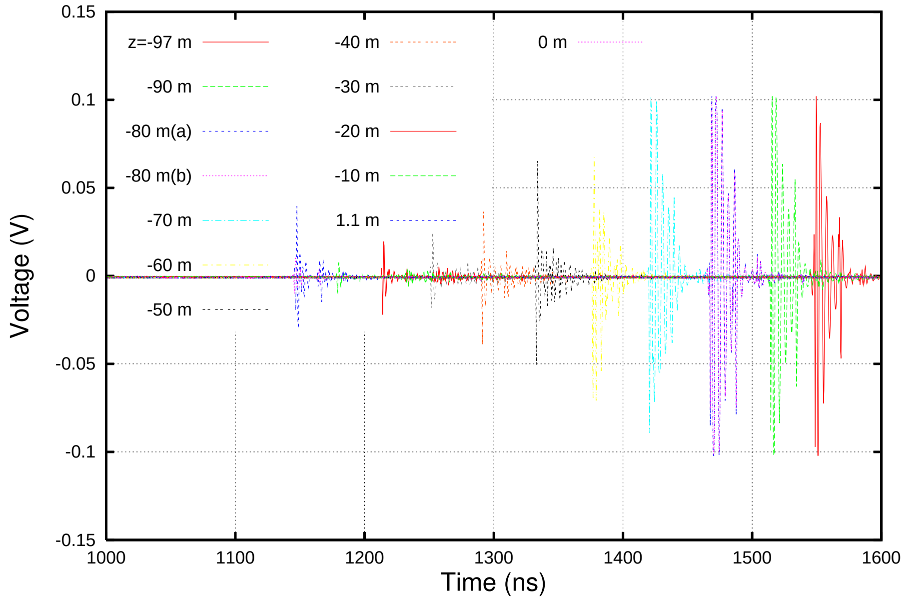

FIG. 41: Signals measured in surface horn as a function of depth of the transmitting discone; radial displacement between Rx and Tx is 70 m. Voltage saturation occurs at $\sim$0.11 V (due to limited dynamic range setting of scope), as evident from the Figure.

Acknowledgments

ANITA is supported under NASA Grant NAG5-5387. We also thank the National Science Foundation's Office of Polar Programs for support under grant NSF OPP-0338219, the Research Corporation, the University of Kansas Undergraduate Research Award Program, and the NSF's Research Experience for Undergraduates (REU) program. We thank the NASA LDB program, and in particular W. Vernon Jones, for providing the support necessary for establishment of our field camp. We thank Phil Austin, RPSC and Fixed Wing support for their superb logistical assistance. Jessica Walker provided important surface and bedrock elevation data while we were in the field. We thank the members of the ITASE traverse for their assistance in establishing our field camp, drilling the hole used for our in-ice transmission, and providing the density data from the borehole. Particulary, we thank Steve Arcone, Daniel Dixon, Paul Mayewski, and Bryan Welch. Bryan Welch also provided essential guidance in assessing the bottom reflection. Ken Ratzlaff of the KU IDL lab provided the instrumentation necessary for the temperature profile measurements. DZB wishes to thank his RICE colleagues for useful conversations regarding the birefringence measurement.

[1] P. B. Price and L. Bergstrom, Applied Optics **36**, 4181-4194 (1997).
[2] S. Barwick, D. Besson, P. Gorham, D. Saltzberg, J. Glac. 04J067 (2005).
[3] I. Kravchenko et al., Phys. Rev. **D73**, 082002 (2006).
[4] `http://geology.cwru.edu/~ansmet/`
[5] S. W. Barwick et al., Phys. Rev. Lett. **96**, 171101 (2006).
[6] J. D. Jackson,*Classical Electrodynamics*, 2nd Ed., John Wiley & Sons, New York (1975).
[7] N. D. Hargreaves, J. Phys. D: Applied Physics 10(9), 1285-1304 (1977).
[8] N. D. Hargreaves, N.D., J. Glac. 21, 301-313 (1978).
[9] K. Matsuoka, T. Furukawa, S. Fujita, N. Maeno N, S. Uratsuka, R. Naruse, O. Watanabe, J. Geophys. Res. 108(**B10**): 24999, doi:10.1029/2003JB002425 (2003).
[10] K. Matsuoka, S. Uratsuka, S. Fujita, F. Nishio, J. Glac. 50(170), 382-388 (2004).
[11] C. Doake et al., Ann. Glac. **34**(1), 165-170 (2002).
[12] C. Doake, H. Corr, H. Coor, A. Jenkins, K. Nichols, C. Stewart, Euro. Space Agency pub. **529**, 313-320 (2003); C. Doake,

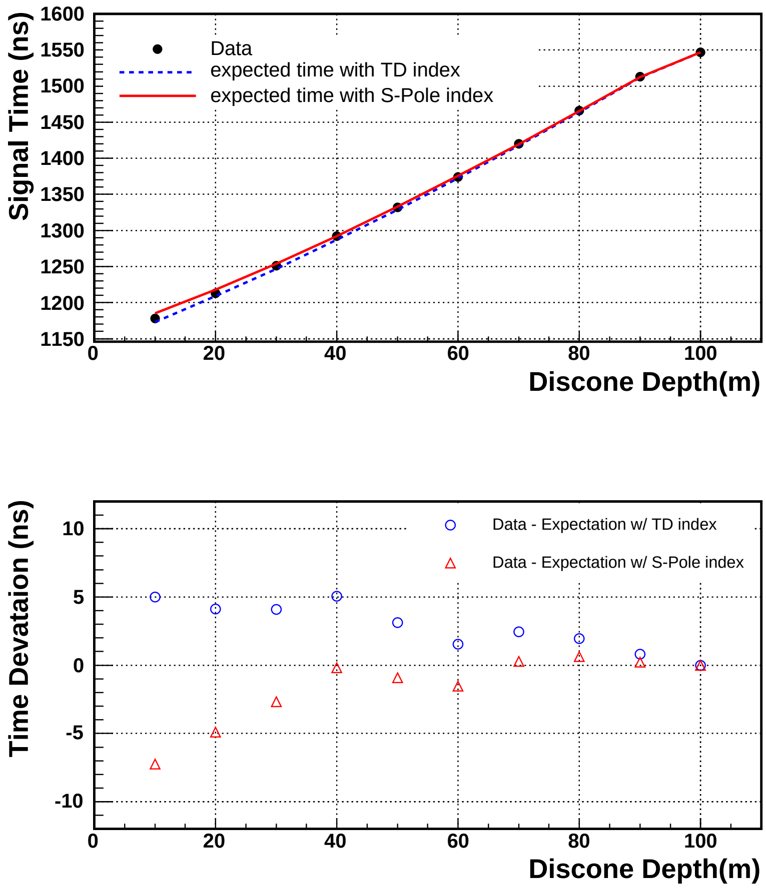

FIG. 42: Comparison of expected vs. measured hit times, assuming index of refraction is related directly to density via Schytt equation.

H. Corr, H. Coor, A. Jenkins, K. Nichols, C. Stewart, FRISP Rep. No. 14 (2003).
[13] A. H. Woodruff and C. S. M. Doake, J. Glac., 23, 223 (1979)
[14] S. Fujita, K. Matsuoka, H. Maeno, T. Furukawa, Ann. Glac 37, 305 (2003).
[15] J. D. Winebrenner et al., Ann. Glac., **37**, 1, 226 (2005)
[16] J. P. Ralston, Phys. Rev. **D71**, 011503(R) (2005).
[17] J. J. Fitzpatrick, Antarctic Journal of the U.S. **29**(5), 84-86 (1994).
[18] D. Dixon, private communication.
[19] B. Welch, private communication.
[20] `www.antarctica.ac.uk/Resources/AEDC/bedmap/`
[21] D. H. M. Millar, Nature, **292**(5822):441, 443 (1981).
[22] V. V. Bogorodsky, C. R. Bentley, and P. E. Gudmandsen, *ed.*, *Radioglaciology.* Dordrecht, Holland, D.Reidel Pub Co., 254 pp. (1985).
[23] B. M. E. Smith. and S. Evans, J. Glac. **11**, (61), 133-146 (1972).
[24] D. M. Rippin, J. L. Bamber, M. J. Siegert, J. of Geophys. Res. 108(F1): 6008, doi:10.1029/2003JF000039 (2003).
[25] S. Fujita, H. Maeno, S. Uratsuka, T. Furukawa, S. Mae, Y. Fujii, and O. Watanabe, J. Geophys. Res. 104(**B6**):13013–13023 (1999).
[26] T. Matsuoka, S. Fujita, S. Morishima and S. Mae, J. Appl. Phys. **81**(5), 2344 (1997).
[27] I. Kravchenko, D. Besson, and J. Meyers, J. Glac. 03J061 (2005).
[28] V. Schytt, Norwegian-British-Swedish Antarctic Expedition, 1949-52, Scientific Results 4, Glaciology 2., Oslo, Norsk Polarinstitutt. 115-151 (1958).
[29] S. Fujita and S. Mae, Ann. Glac. **17**, 269-75 (1993).

[30] S. Fujita et al., J. Glac. **52**(178), 407 (2006).